Astronomy & Astrophysics manuscript no. output
February 3, 2022

On the construction of coronal hole and active region magnetohydrostatic solutions in two dimensions: force and energy balance

J. Terradas[1,2], R. Soler[1,2], R. Oliver[1,2], P. Antolin[3], I. Arregui[4,5], M. Luna[1,2], I. Piantschitsch[1,2,6], E. Soubrié[2,7], and J. L. Ballester[1,2]

[1]Departament de Física, Universitat de les Illes Balears (UIB), E-07122, Spain
[2]Institute of Applied Computing & Community Code (IAC[3]), UIB, Spain
e-mail: jaume.terradas@uib.es
[3]Department of Mathematics, Physics and Electrical Engineering, Northumbria University, Newcastle Upon Tyne, NE1 8ST, UK
[4]Instituto de Astrofísica de Canarias, Vía Láctea s/n, 38205 La Laguna, Tenerife, Spain
[5]Departamento de Astrofísica Universidad de La Laguna, 38206 La Laguna, Tenerife, Spain
[6]Institute of Physics, University of Graz, Universitätsplatz 5, 8010 Graz, Austria
[7]Institut d'Astrophysique Spatiale, CNRS, Univ. Paris-Sud, Université Paris-Saclay, Bât. 121, 91405 Orsay cedex, France

February 3, 2022

ABSTRACT

Coronal holes and active regions are typical magnetic structures found in the solar atmosphere. In the present work we propose several magnetohydrostatic equilibrium solutions representative of these structures in two-dimensions. Our models include the effect of a finite plasma-β and gravity but the distinctive feature is the incorporation of a thermal structure with properties akin to those reported by the observations. We have developed a semi-analytical method to compute the equilibrium configuration. Using this method we obtain cold an underdense plasma structures in open magnetic fields representing coronal holes, while in closed magnetic configurations we achieve the characteristic hot and overdense plasma arrangements of active regions. Although coronal holes and active regions seem to be antagonistic structures, we find that they can be described using a common thermal structure that depends on the flux function. Apart from the force balance, the energy balance is included in the constructed models using an "a posteriori" approach. From the two-dimensional computation of thermal conduction and radiative losses in our models we infer the required heating function to achieve energy equilibrium. We find that the temperature dependence with height is an important parameter that may prevent the system to accomplish thermal balance at certain spatial locations. The implications of these results are discussed in detail.

Key words. Magnetohydrodynamics (MHD) — Sun: magnetic fields

1. Introduction

Coronal holes (CH) are usually defined as the darkest patches on the solar surface observed in ultraviolet (UV) and X-ray radiation. These structures are associated with magnetic fields open to the interplanetary space and have strong links with the solar wind, supposed to emanate from their base. A significant effort over the last decades of part of the scientific solar community has been to reproduce the velocities reported in the solar wind. The reader is referred to the review of Cranmer (2009) about measurements of the plasma properties in coronal holes and how they are used to reveal details about the physical processes that heat the solar corona and accelerate the solar wind. Because the magnetic field in CHs is unipolar and therefore open, this configuration is, in some aspects, similar to solar sunspots (see a detailed comparison in Obridko & Solov'ev 2011) characterised by a concentration of magnetic flux at a low temperature with respect to the environment. However, CHs are supposed to have a low plasma-β (ratio of gas to magnetic pressure) in contrast to sunspots where this parameter changes substantially with height when moving from the photosphere to the corona. The plasma-β is typically around 3×10^{-3} in coronal holes (see for example Isenberg & Vasquez 2007).

The inverse arrangements to CHs are active regions (AR), composed of dense and hot plasma cores lying along closed magnetic field lines. UV-imaging spectroscopy during the early 1970s from Skylab already revealed that active regions are composed of filamentary structures, commonly called loops, rather than consisting of a plain diffuse plasma distribution. Gallagher et al. (2001) found that the active region they studied had the structure of a central hot high-density core, contained by a large number of low-lying magnetic field lines and surrounded by cooler loops, which were in turn embedded in hot coronal plasma. These authors were able to estimate the plasma pressure distribution over the active region and found that it is higher in the core and lower in the halo (almost two orders of magnitude), this is in agreement with the fact that in active regions pressure is known to be correlated with higher magnetic flux concentrations, see for example Golub et al. (1980). It is also known that the magnetic field is a primary quantity in relation to coronal heating, specially in ARs. Although the analysis and modeling of coronal loops in active regions has received a lot of attention (see for example Aschwanden et al. 1999, 2000) the plasma emitting in EUV within the AR that is not associated with distinguishable loops is often ignored. Here we concentrate

on the largely diffuse component in active regions since coronal loops generally comprise only a small proportion of the AR emission, typically only 10%–30% of enhancements over the "background" (Del Zanna & Mason 2003 and Viall & Klimchuk 2011). In our case, and similar to the definition given in Viall & Klimchuk (2011), diffuse emission refers to background emission where there are no distinct discrete intensity enhancement such as loops, and whether it occurs in hot or warm temperatures. One of the conclusions of the work of Viall & Klimchuk (2011) is that the diffuse background shows understandable patterns consistent with impulsive nanoflare heating. This indicates that the emitting coronal plasma in the whole AR is not steady, it is dynamic and constantly evolving (see also Viall & Klimchuk 2012, 2016, 2017). This is somehow in contradiction with the results of Warren et al. (2012) that indicate that the hot component plasma in several observed ARs is often close to equilibrium. Recently, Warren et al. (2020) have shown, using observations of an AR from the High-resolution Coronal Imager (Hi-C) sounding rocket together with modeling, that the heating in the active region core is taking place at a relatively high frequency and that the observed loops are close to equilibrium. This is a hint of nearly steady heating.

A common approach used in the literature regarding heating studies in the solar corona relies on the assumption of an "a priori" form of the heating, for example, a decaying exponential with height. Such heating profile, representing a footpoint heating, has been used to solve the time-dependent problem and the characteristics of the equilibrium, if achieved, or of the non-equilibrium, have been investigated in detail in the past (see for example the summaries on this subject of Klimchuk 2019 and Antolin 2020). Thermal nonequilibrium (TNE) is a clear example of a non existing equilibrium situation where a nonlinear mechanism can explain coronal rain or the cold condensations that lead to prominence formation around magnetic dips. The "a priori" approach about the heating form is not the only way to tackle this problem. An alternative method is based on the calculation of the stationary solutions of the configuration in two or three dimensions. Under this approach we have the possibility of choosing a certain temperature and pressure profile, calculate the force balance to have equilibrium of forces, and investigate "a posteriori" the energy balance without an "a priori" assumption about the heating form. The choice of temperature and pressure, together with the magnetic field, determine thermal conduction in the system. The optically thin radiative losses of the corona depend on the density and temperature distribution of the obtained solution under force balance. Once we have the contribution of thermal conduction and radiative losses we can calculate the heating profile to have a perfect equilibrium. An example of this is the 1D equilibrium achieved by loops that satisfy the RTV scaling law (see the model of Rosner et al. 1978 under the assumption of uniform pressure and heating and also the 2D model of Petrie et al. 2003). The question that arises here is whether we can always find energy balance in the system. With this approach we can derive, without directly solving the time-dependent problem, some conditions that lead to the existence of thermal balance or not. In this case thermal balance does not refer to thermal equilibrium along an individual magnetic field line only (the 1D case), since the problem is treated in two dimensions in the present work, we consider CHs or ARs as global structures instead.

Either if the coronal heating is impulsive or steady, it is known that many magnetic structures of the solar corona can have, from a large scale point of view, long lifetimes suggesting that they are in a sort of equilibrium state, although the observations reveal a strong dynamism often reinforced by the presence of flows on small spatial scales. In spite of the dynamic nature of the coronal structures, magnetohydrostatic (MHS) models, where flows are assumed to be zero or stationary, should not be discarded. In particular, there is a lack of recent literature on MHS equilibrium models of coronal holes, except the works of Tsinganos (1981, 1982); Low & Tsinganos (1986) in the 80s, and the aforementioned work of Obridko & Solov'ev (2011). MHS models of coronal holes are needed for several reasons. They can provide a better understanding of how these structures are kept in the two basic balance conditions, namely the force and thermal balance. MHS models of CHs are necessary for other purposes such as for example to carry out investigations about the interaction of global MHD waves with these structures since so far, very simple geometries have been addressed, mostly based on purely vertical magnetic field (see Piantschitsch et al. 2018a,b, 2020 and Piantschitsch & Terradas 2021). Global 3D MHD simulations have been also used to investigate this problem (e.g. Downs et al. 2011) but the results about the interaction with CHs are limited and deeper analysis are required specially using elementary models. The same also applies to the construction of magnetohydrostatic solutions of ARs. Another argument in favor of studying MHS models is that we can get some information about the conditions for which these models are not possible. In order words, if the MHS models provide unrealistic configurations, this means that real solar structures are not in MHS equilibrium.

The main aim of the present work is dual. First, we explore different CH models that include a cold and under-dense region (the CH) that connects with an atmosphere at typically 1 MK (corona) through a smooth coronal hole boundary (CHB). Using the same scheme based on the early works of Low (1975, 1980), we investigate how uninvolved MHS models can also reproduce the main features of ARs, paying special attention to the high pressure and diffuse background of these structures instead of the single loop structures. The main characteristics of the different MHS models developed here are analysed in detail. Second, and closely related to the previous goal, we carry a detailed investigation about the energy balance in these structures. We calculate the spatial distribution of heating necessary to have a situation under thermal balance and we provide some constraints on the temperature dependence with height to achieve energy equilibrium.

2. The problem of magnetohydrostatic equilibrium in 2D

We start by describing the problem we aim to solve and how it is formulated using the equations of the magnetohydrostatics, applicable as a first approach to CHs and ARs. Low (1975) addresses the situation of magnetohydrostatic equilibrium under the presence of purely vertical gravity in Cartesian geometry. The reader is also referred to the works of Parker (1968) (see their Appendix A) and Parker (1979). We look for solutions to the following equation

$$\frac{1}{\mu_0}(\nabla \times \mathbf{B}) \times \mathbf{B} - \nabla p - \rho g\, \hat{\mathbf{e}}_\mathbf{z} = 0, \tag{1}$$

where $\mathbf{B}$ is the magnetic field, p is the gas pressure, ρ the plasma density, g the gravity acceleration on the solar surface (pointing in the negative $z-$direction) and μ_0 the magnetic permeability of free space. The magnetic field from Maxwell's equations has to

satisfy that

$$\nabla \cdot \mathbf{B} = 0. \tag{2}$$

We suppose that the plasma is composed of fully ionised hydrogen that satisfies the ideal gas law

$$p = \frac{\mathcal{R}}{\bar{\mu}} \rho T, \tag{3}$$

where T is the temperature, $\mathcal{R}$ the gas constant, and $\bar{\mu}$ the mean atomic weight ($\bar{\mu} = 0.5$ for fully ionized hydrogen plasma and $\bar{\mu} = 0.6$ when fully ionized helium with coronal abundances is included). The aim is to obtain solutions to the previous equations but we have a system of five equations (Eqs. (1)-(3)) but six unknowns, $\mathbf{B}$ (three components), p, ρ and the temperature T. An energy equation, or sometimes termed as the heat transport equation, is required to have a closed system. Here we adopt the approach of Low (1975) in which the energy equation is not solved directly. The key point is to select a temperature profile based on some observational constraints, in particular we use the fact that in coronal holes the plasma temperature is lower than in the coronal environment, see Munro & Withbroe (1972) and the references in Cranmer (2009). Once we have obtained a solution we calculate the corresponding energy balance that the system has to satisfy in order to keep a thermal equilibrium. Since the energy equation is not easy to be solved simultaneously with force balance, another option is to prescribe a priori a polytropic equation of state, which effectively corresponds to some energy addition/sink computed a posteriori (e.g. Tsinganos et al. 1992 and Petrie et al. 2002). Nevertheless, here we prefer to select an "a priori" temperature profile based on some observational constraints.

To avoid unnecessary complications we restrict our analysis to a two-dimensional coordinate geometry with invariance in the $y-$direction and with no component of the magnetic field in this direction. The magnetic field is written in terms of a magnetic flux function (the $y-$component of the magnetic vector potential), denoted by $A(x, z)$ and ensuring Eq. (2), but that needs to be determined. We write

$$B_x(x, z) = -\frac{\partial A}{\partial z}(x, z), \tag{4}$$

$$B_y(x, z) = 0, \tag{5}$$

$$B_z(x, z) = \frac{\partial A}{\partial x}(x, z). \tag{6}$$

The dependence of gas pressure and temperature with the magnetic flux function is prescribed according to the type of solution that we are seeking for. It can be shown, see for example Low (1975), Priest (1982) and the multiple examples explored in Priest & Forbes (2007), that the flux function is the solution of the following nonlinear elliptical partial differential equation

$$\frac{\partial^2 A}{\partial x^2}(x, z) + \frac{\partial^2 A}{\partial z^2}(x, z) + \mu_0 \frac{\partial p(A, z)}{\partial A} = 0, \tag{7}$$

where gas pressure is given by

$$p(A, z) = p_0(A)\, e^{-\int_0^z \frac{\bar{\mu} g}{\mathcal{R} T(A, z')}\, dz'}, \tag{8}$$

and $T(A, z)$ is the temperature profile that can depend on the flux function A and the z coordinate as well. Equation (8) imposes a balance between the force due to the gas pressure gradient and the gravity force along the magnetic field lines, while Eq. (7) represents the condition of force balance perpendicular to the magnetic field. The function $p_0(A)$ determines the profile of gas pressure at $z = 0$. Equation (7) is of Grad-Shafranov type but includes the effect of gravity. This equation must be solved under some boundary conditions.

It is useful to rewrite Eq. (7) in dimensionless form, since it reduces to

$$\frac{\partial^2 \bar{A}}{\partial \bar{x}^2}(\bar{x}, \bar{z}) + \frac{\partial^2 \bar{A}}{\partial \bar{z}^2}(\bar{x}, \bar{z}) + \frac{\beta_0}{2} \frac{\partial \bar{p}(\bar{A}, \bar{z})}{\partial \bar{A}} = 0, \tag{9}$$

where

$$\beta_0 = \frac{2\mu_0 p_{00}}{B_0^2} \tag{10}$$

is the reference plasma-β, the lengths are normalized to h, pressure to p_{00} and the flux function to $B_0 h$. The pressure scale height is $h = \mathcal{R} T_C / \bar{\mu} g$, where T_C is the reference coronal temperature (h is typically of the order of 60 Mm for $T_C = 1$ MK). If gas pressure is ignored in Eq. (9) ($\beta_0 = 0$) this equation reduces to a Laplace equation that leads to the potential solution. In this case a maximum principle exists stating that a solution cannot attain a maximum (or minimum) at an interior point of its domain. This result implies that the values of the solution in a bounded domain are bounded by its maximum and minimum values on the boundary.

The magnetic field and the thermodynamic variables are given in terms of A, $p_0(A)$ and $T(A, z)$. We make a distinction between the photospheric and coronal footpoint definition, which can be quite different in case of a canopy-like divergence from the phothosphere to the base of the corona. Our reference level, $z = 0$, is located at the base of the corona. If we know the magnetic field at this reference level, i.e., $B_z(x, z = 0)$, then we calculate the flux function at this level by direct integration of Eq. (6),

$$A(x, z = 0) = \int B_z(x, z = 0)\, dx, \tag{11}$$

which is used to calculate gas pressure at the reference level

$$p(x, z = 0) = p_0(A(x, z = 0)). \tag{12}$$

We need to solve Eq. (7) subject to the boundary value of $A(x, z = 0)$ (a Dirichlet problem) previously calculated, and in terms of some given $T(A, z)$ that has not been prescribed yet. The most relevant boundary condition is at the bottom of the system, $z = 0$, this determines the behaviour of the solution on the whole spatial domain. The Grad-Shafranov equation is a fourth order partial differential equation meaning that we have to specify additional boundary conditions. We have explored two situations, a finite rectangular domain and the upper half-plane (with the solution assumed to vanish at infinity), and have decided to concentrate in the last configuration because it is not affected by the location of the edges of a finite domain.

It is worth mentioning that Low (1980) proposed another scheme in which treating $A(x, z)$ as a known function then Eq. (7) is used to determine $T(A, z)$. This scheme is more flexible and the equations of magnetostatic equilibrium can be readily integrated in closed form. However, for the purposes of the present paper related to the investigation of different profiles for $T(A, z)$, the scheme of Low (1975) adopted here is more convenient.

3. Magnetic configuration

In this section we present how the magnetic field configuration is calculated. We begin with the most uncomplicated case, a unipolar magnetic field that represents a coronal hole and then we

explore a bipolar model describing an AR. We provide rather simple analytical solutions in the case $\beta = 0$, i.e., the potential magnetic field.

3.1. The unipolar coronal hole and the bipolar active region

The type of solutions we are interested in should represent a coronal hole and the boundary conditions at $z = 0$ allow us to chose families of solutions that have a vertical magnetic field at the center of the hole that progressively expands with distance from the central part. This is the sort of configuration that is inferred from the observations and from photospheric magnetic field extrapolations. A convenient choice is a function that is concentrated at $x = 0$ and that decreases with distance, for example following a Gaussian dependence:

$$B_z(x, z = 0) = B_0\, e^{-\left(\frac{x}{w_0}\right)^2}, \tag{13}$$

where w_0 is the characteristic width and the Gaussian is centered around $x = 0$. Integrating with respect to x, Eq. (11), we find that the corresponding flux function is

$$A(x, z = 0) = \frac{\sqrt{\pi}}{2} B_0 w_0\, \mathrm{Erf}\left(\frac{x}{w_0}\right) + C, \tag{14}$$

where $\mathrm{Erf}(x)$ is the error function and C is an integration constant that is set to zero with no loss of generality. The obtained flux function is proportional to the product $B_0\, w_0$ and to the error function which is very similar to the hyperbolic tangent function. An example of the flux function is shown in Fig. 1. It is worth noting that although the magnetic field is localized in space the flux function is not confined around $x = 0$ and it has tails that extend over the whole spatial domain. This is due to the fact that the magnetic field is unbalanced, i.e., the net magnetic flux is not zero.

Other profiles for the magnetic field can be explored, but as we show in the following, the main features of the flux function are found to be essentially the same. Let us consider an inverse parabolic profile for the magnetic field,

$$B_z(x, z = 0) = \begin{cases} B_0 - B_0 \left(\frac{x}{x_0}\right)^2 & -x_0 < x < x_0, \\ 0 & |x| \geq x_0. \end{cases} \tag{15}$$

The corresponding flux function is

$$A(x, z = 0) = B_0 F(x) = \begin{cases} B_0 x - \frac{B_0}{x_0^2}\frac{x^3}{3} & -x_0 < x < x_0, \\ \frac{2}{3} B_0 x_0 & x \geq x_0, \\ -\frac{2}{3} B_0 x_0 & x \leq -x_0, \end{cases} \tag{16}$$

where the values of $A(x, z = 0)$ for $|x|$ larger or equal than x_0 (we assume that $x_0 > 0$) have been adjusted through the integration constant to have a continuous derivative of A and therefore a continuous variation of $B_z(x, z = 0)$. The integration constant C has been also set to zero. We have introduced the definition of $F(x)$ in Eq. (16). The flux function is plotted in Fig. 1 and can be compared with the corresponding flux function associated to the Gaussian profile. The two profiles are very similar, meaning that for our purposes we do not have to worry about the specific function we chose to represent the unipolar magnetic field. In the rest of this section we use the parabolic profile for the magnetic field and the corresponding flux function. The reason of choosing this dependence relies in the fact that, as we show later, analytical progress is possible if the polynomial form of the flux function given by Eq. (16) is used. When the energetics of the problem is addressed in Sect. 5 the Gaussian profile is more convenient since the conduction term (involving second order spatial derivatives) has a smoother behaviour than for the parabolic profile (which has discontinuous derivatives in the $x-$direction).

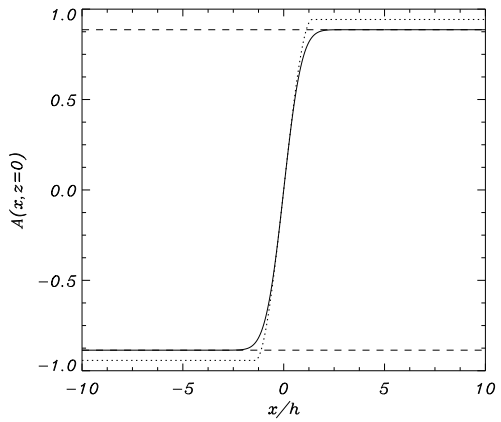

Fig. 1. Flux function as a function of the horizontal position at $z = 0$. Continuous line corresponds to the Gaussian profile and the dotted line to the parabolic profile. The horizontal dashed lines represent the constant values that the Gaussian profile tends asymptotically. In this plot $w_0/h = 1$, and $C = 0$ for the Gaussian profile, while $x_0/h = 1$ for the parabolic profile.

Now we aim at constructing an elementary magnetic model that represents an active region. Such configurations are in general bipolar and a straightforward method to represent them is to superpose two individual unipolar regions of opposite polarity and separated a certain distance, in terms of the function $F(x)$ introduced before, the flux function is

$$A(x, z = 0) = B_1 F(x - x_1) + B_2 F(x - x_2), \tag{17}$$

where we assume hereafter that $B_1 B_2 < 0$ to have a bipolar configuration. The parameters x_1 and x_2 correspond to the centers of the opposite polarity unipolar magnetic fields, the distance between them is therefore $|x_1 - x_2|$. If we assume that the two unipolar regions are equal (same widths and intensities, except the sign of the magnetic field), then the flux function, contrary to the case of a unipolar field, is a localized function in space. In this situation there is a perfect balance that cancels the tails of the flux function, this feature is clear in Fig. 2.

In a general case it is not difficult to see that the minimum and maximum values of the flux function are given by

$$A_{min} = (-B_1 x_0 - B_2 x_0)\, \frac{1}{2}, \tag{18}$$

while the absolute maximum value is

$$A_{max} = (B_1 x_0 - B_2 x_0)\, \frac{1}{2}. \tag{19}$$

We have assumed that the thickness of each unipolar region is the same, x_0, but the previous expressions are easily extended to non equal widths. The minimum and maximum values of the flux function are useful when the thermal structure of the model is introduced later in Sect. 4.

3.2. Solution for the upper half-plane: Green's function

For the situation $\beta = 0$ we have seen that the Grad-Shafranov equation given by Eq. (7) reduces to a Laplace equation. Suppose that the domain is $z > 0$ (upper half-plane) and therefore

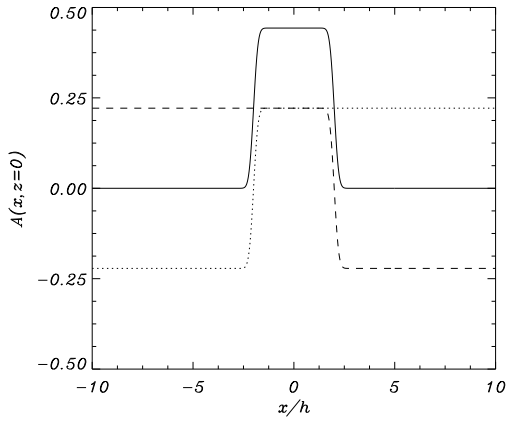

Fig. 2. Flux function as a function of the horizontal position at $z = 0$ for the bipolar active region described by Eq. (17). The continuous line corresponds to the superposition of the left unipolar region (dotted line) and the right unipolar region (dashed line). In this plot $x_1/h = -2$, $x_2/h = 2$ and $x_0/h = 1/4$.

we do not have to concern about the boundary conditions in the $x-$direction and the upper boundary. For this kind of problem it is known that we can use the properties of Green's functions. Indeed, they have been applied in the past to calculate potential magnetic fields based on photospheric magnetograms (the reader is referred to Schmidt 1964 and Sakurai 1982 for details about the first applications of the Green's function method in the solar context). Using this method it is known that the Laplace equation in the Cartesian domain $z > 0$ plus the inhomogeneous boundary condition at $z = 0$ has the following analytical solution

$$A_0(x,z) = \frac{z}{\pi}\int_{-\infty}^{\infty} \frac{A(\xi, z=0)}{(x-\xi)^2+z^2}\, d\xi, \tag{20}$$

where we use the subindex 0 to indicate that it corresponds to the zero beta case. This exact solution tends to zero at large distances from the source, and involves a definite integral and the specific profile of the flux function at $z = 0$, i.e., $A(x, z = 0)$. In general the integral in Eq. (20) needs to be calculated numerically but for our deliberate choice of the parabolic profile for the unipolar field at $z = 0$ given by Eq. (16), the primitive is analytical,

$$\begin{aligned} A_0(x,z) = \frac{a_0}{4\pi x_0^3}\Bigg(& z\left(-3x^2+3x_0^2+z^2\right)\ln\frac{(x-x_0)^2+z^2}{(x+x_0)^2+z^2} \\ &+\left(2x^3-6xx_0^2-6xz^2+4x_0^3\right)\tan^{-1}\left(\frac{x-x_0}{z}\right) \\ &+\left(-2x^3+6xx_0^2+6xz^2+4x_0^3\right)\tan^{-1}\left(\frac{x+x_0}{z}\right)-8xx_0z\Bigg), \end{aligned} \tag{21}$$

where $a_0 = (2/3)x_0B_0$. This solution contains up to third order polynomials together with logarithmic and trigonometric functions and it is therefore relatively easy to handle. It can be shown that applying l'Hôpital's rule, the limit of Eq. (21) when z tends to ∞ is zero, as expected.

The components of the magnetic field associated to Eq. (21) are, using Eqs. (4) and (6),

$$\begin{aligned} B_x(x,z) = \frac{3a_0}{4\pi x_0^3}\Bigg(& 4xx_0+\left(x^2-x_0^2-z^2\right)\ln\frac{(x-x_0)^2+z^2}{(x+x_0)^2+z^2} \\ &+4xz\left[\tan^{-1}\left(\frac{x-x_0}{z}\right)-\tan^{-1}\left(\frac{x+x_0}{z}\right)\right]\Bigg), \end{aligned} \tag{22}$$

$$\begin{aligned} B_z(x,z) = -\frac{3a_0}{2\pi x_0^3}\Bigg(& 2x_0z+xz\ln\frac{(x-x_0)^2+z^2}{(x+x_0)^2+z^2} \\ &+\left(-x^2+x_0^2+z^2\right)\left[\tan^{-1}\left(\frac{x-x_0}{z}\right)-\tan^{-1}\left(\frac{x+x_0}{z}\right)\right]\Bigg). \end{aligned} \tag{23}$$

Substituting $z = 0$ in Eq. (23) and using that $\tan^{-1}(\pm\infty) = \pm\pi/2$ we find that only the third term on the right-hand side is different from zero, and we recover the parabolic profile given by Eq. (15) used as boundary condition to construct the solution in the whole two-dimensional domain.

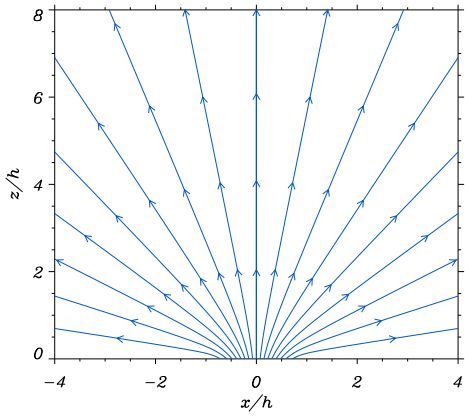

Fig. 3. Magnetic field lines in the analytical CH model given by Eq. (21) ($\beta_0 = 0$). In this example the half width of the CH at $z = 0$ is $x_0 = h$. Magnetic field lines coincide with isocontours of the flux function A_0. Note that the geometry of the magnetic field would be affected by the presence of boundaries at a finite distance from the source but the method implemented in this work through the Green's functions prevents such effects.

An example of a CH model based on the previous analytical solution is shown in Fig. 3 for a particular choice of the parameters B_0 and x_0. The magnetic field is purely vertical at $x = 0$ and globally showing radial expansion of straight magnetic field lines except near the bottom boundary where the field matches the boundary conditions at $z = 0$ and the magnetic field lines are slightly curved. At low heights and far from the source, the horizontal component of the magnetic field is dominant over the vertical component. In fact since at $z = 0$ we impose that $B_z(x, 0) = 0$ for $|x| \geq x_0$ (see Eq. (15)) the magnetic field becomes purely horizontal at our reference level. In this regard the Gaussian profile given by Eq. (13) would avoid such effect and produce a more confined structure. In a real CH it is quite unlikely that the magnetic field is purely horizontal outside the CH because there are contributions from other nearby magnetic fields with different spatial scales and intensities that have emerged through the photosphere (this is partially addressed in the following paragraphs where a CH is combined with an AR).

The analytical solution for the unipolar magnetic field is the basis to construct more complicated magnetic configurations. As we have mentioned in the previous section we build an AR model by adding two unipolar magnetic fields of opposite polarity. We can use this superposition of solutions for the flux function because the Laplace equation is a linear partial differential equation. We introduce a translation of the solution given by Eq. (21) with respect to the $x-$coordinate by making the change $x \rightarrow (x - x_1)$, being x_1 the center of the new unipolar region. We do the same operation for the opposite polarity unipolar field, located at x_2 and then we add the corresponding flux functions according to Eq. (17). An example of such equilibrium is shown in Fig. 4. We obtain closed field lines that for our purposes represent a typical magnetic configuration of a symmetric bipolar AR. This magnetic configuration is used later to host a dense and hot plasma in the case of a plasma-β different from zero. Figure 5 shows a similar situation but the AR is not perfectly symmetric being the magnetic field at the right footpoint stronger than that at the left footpoint. At low heights the configuration is closed but changes to open as we move away from the AR core. At very large distances from the bipolar region we essentially recover the structure of a single unipolar configuration with straight magnetic field lines, compare with Fig. 3.

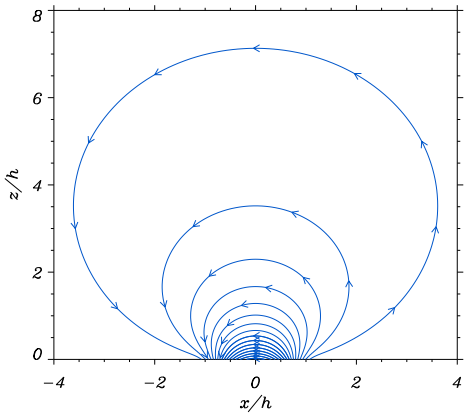

Fig. 4. Magnetic field lines in a symmetric AR model based on Eq. (17). In this example the two unipolar sources are located at $x_1 = -1/4h$ and $x_2 = 1/4h$ being $x_0 = h$.

Two additional examples of equilibrium based on the superposition of unipolar regions are shown in Fig. 6. The magnetic configuration combines a CH and an AR together. In the first case the polarity of the left footpoint of the AR is the same as the polarity of the CH. The CH is displaced towards the left due to the presence of the AR which is squashed by the CH. Due to the presence of AR the magnetic field is no longer purely horizontal at the right part of the CH for $x > x_0$ as happens in the configuration of Fig. 3. In the second situation the polarity of the AR is reversed. The CH is shifted to the right and a null or X-point, with zero magnetic field, appears in the AR. Indeed, in such a configuration the separatrixes of the magnetic field provide an excellent definition of the location of the CHB (understood as the layer that separates open from closed magnetic field lines). In conclusion, the examples shown in this section illustrate the flexibility of the scheme to construct a variety of potential magnetic field configurations that can be used in general as the basis for other studies, and in particular in the following section as the skeleton to include the effect of gas pressure and gravity in the system.

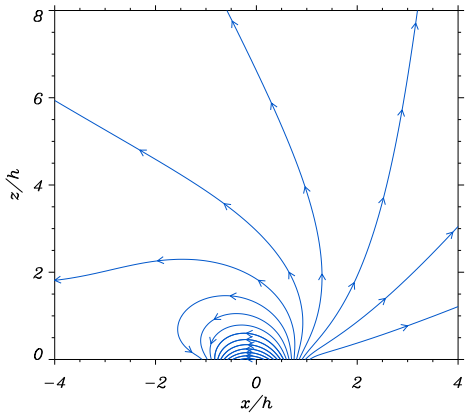

Fig. 5. Magnetic field lines in a non-symmetric AR model. In this example the two unipolar sources are located at $x_1 = 1/4h$ and $x_2 = -1/4h$ being $x_0 = h$. The source located at $x = x_1$ is 1.2 times stronger than the source at $x = x_2$. There is some spatial overlap in the sources but this is allowed in our model since it is based on the superposition of individual solutions.

4. Coupling the magnetic field to the plasma

When the β of the plasma is different from zero the magnetic field and the plasma are coupled. Since in coronal holes, active regions, and in general in the corona this parameter is small, the deviation from the potential solution is expected to be limited. Nevertheless, including gas pressure in the scheme is crucial because the observations specifically provide information about the structure in density (emission measure) and temperature (both related to gas pressure), and to a lesser extend about the magnetic field, inferred from extrapolations based on photospheric magnetograms.

In our model we include a non-zero gas pressure in Eq. (7) through the, in principle, arbitrary functions $p_0(A)$ and $T(A, z)$ that need to be defined. For simplicity and with the aim of focusing on the overall behaviour, we assume the following separable dependence for temperature, although this is not mandatory in the present formalism,

$$T(A, z) = \mathcal{T}(A)\mathcal{H}(z). \tag{24}$$

This profile entails a type of uniform temperature dependence with height in the whole region of interest, either the CH or AR, but temperature is still allowed to vary from field line to field line due to the term $\mathcal{T}(A)$. This is a situation similar to the cases of self-similar MHD solutions explored, for example, by Petrie et al. (2002, 2003) and Tsinganos (2010). An isothermal temperature distribution along a given field line (A = const) is obtained by imposing that $\mathcal{H}(z) = 1$. In this case, and according to Eq. (8), the gas pressure dependence is

$$p(A, z) = p_0(A)\, e^{-\frac{\bar{\mu} g}{\mathcal{R}\mathcal{T}(A)} z}. \tag{25}$$

which is the well known exponential stratification whose scale height depends on the temperature of the plasma along the field line that we are considering (the particular value of A).

For the nonisothermal situation a simple choice for the temperature dependence with height is

$$\mathcal{H}(z) = e^{z/\Lambda}, \tag{26}$$

being Λ the characteristic spatial scale which might be positive or negative. This allows us to consider a situation with an

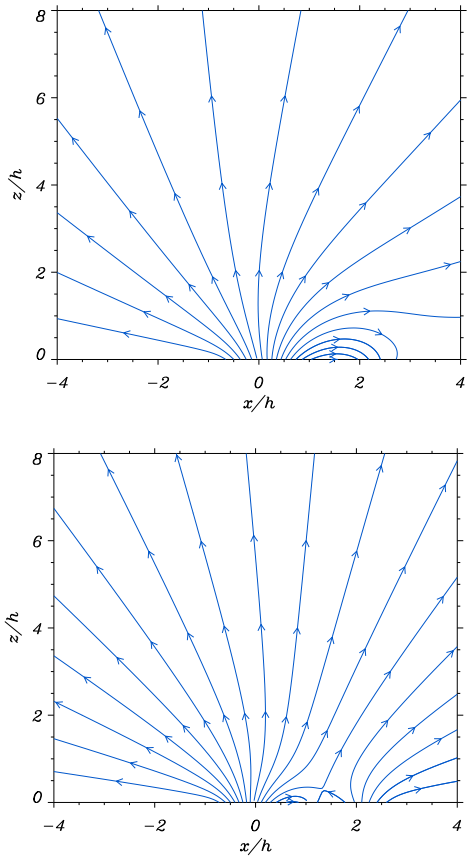

Fig. 6. Magnetic field lines of a mixed CH and AR model. The CH is located at $x_1 = 0$ while the AR is represented by equal opposite polarity sources located at $x_1 = h$ and $x_2 = 2h$ being $x_0 = h$. The differences between the two panels are due to the polarity of the left footpoint of the AR with respect to the CH, in the left panel positive while in the right panel it is negative, leading to the creation of an X-point.

increasing or decreasing temperature with height and therefore with a net effect of thermal conduction that changes the energy balance in the system, addressed in Sect. 5. The pressure dependence in the nonisothermal case calculated from Eq. (8) is

$$p(A,z) = p_0(A)\, e^{\frac{\bar{\mu}g}{\mathcal{R}\mathcal{T}(A)}\Lambda\,(e^{-z/\Lambda}-1)}, \tag{27}$$

and deviates from the easy exponential dependence with z for the isothermal situation, Eq. (25).

According to these equations the gas pressure term that appears in Eq. (7) reads, for the isothermal case (hereafter when we refer to an isothermal situation we mean that temperature does not change along the magnetic field lines, but it changes from line to line)

$$\frac{\partial p}{\partial A}(A,z) = e^{-z\frac{\bar{\mu}g}{\mathcal{R}\mathcal{T}(A)}}\left(\frac{\partial p_0}{\partial A}(A) + z\frac{\bar{\mu}g}{\mathcal{R}}\frac{\partial \mathcal{T}}{\partial A}(A)\frac{p_0(A)}{\mathcal{T}^2(A)}\right), \tag{28}$$

while for the nonisothermal case, using Eq. (27), we simply use the transformation

$$z \rightarrow -\Lambda\,(e^{-z/\Lambda}-1), \tag{29}$$

since the derivatives in Eq. (28) do not affect the z coordinate explicitly.

4.1. Coronal hole and active region thermal structure

Once we know some general features of the pressure and temperature dependence in our model we must constrain the functional form of $p_0(A)$ and $\mathcal{T}(A)$ according to observations of CH and AR. For the CH model we chose these functions to have a minimum at the center of the structure and to increase smoothly with position to match coronal values, creating a depletion in pressure and temperature inside the CH. This is the common behaviour inferred from observations of CH (see for example Cranmer 2009). Our specific choice is

$$p_0(A) = (p_{\rm C} - p_{\rm CH})\left(\frac{A}{A_{ref}}\right)^2 + p_{\rm CH},$$
$$\mathcal{T}(A) = (T_{\rm C} - T_{\rm CH})\left(\frac{A}{A_{ref}}\right)^2 + T_{\rm CH}, \tag{30}$$

where $p_{\rm C}$ and $T_{\rm C}$ are the reference coronal pressure and temperature values outside the coronal hole and $p_{\rm CH}$ and $T_{\rm CH}$ are the values inside the CH (satisfying that $p_{\rm CH}/p_{\rm C} < 1$ and $T_{\rm CH}/T_{\rm C} < 1$ to have representative CH conditions). In Eq. (30) the dependence with the square of the flux function, A, is because firstly, pressure and temperature must be positive defined (and A is not necessarily positive everywhere, see Fig. 1) and secondly, the unipolar region should be symmetric with respect to the center of the CH because the magnetic field is symmetric (the parabolic profile). The quadratic dependence satisfies these requirements but this is not a unique possible choice. In Eq. (30) the flux function A is divided by a reference value, A_{ref}, which in this present case is chosen to be equal to A_{min}, previously introduced in Sect. 3.1. This allows us to fix coronal values to $p_{\rm C}$ and $T_{\rm C}$ for $A = A_{min}$. The values of $p_{\rm CH}$ and $T_{\rm CH}$ are achieved when $A = 0$, i.e., when the magnetic field is vertical in our configuration. Applying the ideal gas law we obtain the relation

$$\frac{\rho_{\rm CH}}{\rho_{\rm C}} = \frac{p_{\rm CH}}{p_{\rm C}}\frac{T_{\rm C}}{T_{\rm CH}}, \tag{31}$$

which must be smaller than one to represent a coronal hole (underdense structure with respect to the environment). This means that we have the restriction $p_{\rm CH}/p_{\rm C} < T_{\rm CH}/T_{\rm C}$ when choosing the parameters of the CH model, i.e., the pressure decrement must be smaller that the temperature decrement.

Other profiles in Eq. (30) can be adopted, but the important property is that the central values must be smaller than the coronal values to properly represent coronal hole conditions. It is necessary to remark that if we assume a constant temperature along field lines, then thermal conduction, in principle relevant in the solar corona, would not have any effect, since it is proportional to the second derivative of temperature with space which is zero in this particular case.

The question that arises now is how we can define the dependence of pressure and temperature when an active region is considered. ARs are denser and hotter than the surrounding corona. According to the dependence of the flux function on position in a bipolar AR, see Fig. 2, a suitable choice is

$$p_0(A) = (p_{\rm AR} - p_{\rm C})\left(\frac{A}{A_{ref}}\right)^2 + p_{\rm C},$$
$$\mathcal{T}(A) = (T_{\rm AR} - T_{\rm C})\left(\frac{A}{A_{ref}}\right)^2 + T_{\rm C}. \tag{32}$$

We could select a linear dependence with A instead, but if the bipolar region has a small imbalance in the parameters B_1 and

B_2 then the flux function can be negative and this is not convenient to ensure positive defined pressures and temperatures. With a quadratic dependence we avoid these issues. Using Eq. (32) when $A = 0$ pressure and temperature have exactly coronal values, p_C and T_C. At the center of the active region we have that $A = A_{ref}$ and therefore pressure and temperature tend to the core values, p_{AR} and T_{AR} ($p_{AR}/p_C > 1$ and $T_{AR}/T_C > 1$ to describe an AR). For a symmetric bipolar region we have that $A_{ref} = A_{max}$ and $A_{min} = 0$. Again, from the ideal gas law we find that

$$\frac{\rho_{AR}}{\rho_C} = \frac{p_{AR}}{p_C}\frac{T_C}{T_{AR}}, \tag{33}$$

which must be greater than one to represent an overdense region with respect to the environment. Therefore, the condition $p_{AR}/p_C > T_{AR}/T_C$ needs to be satisfied.

From Eqs. (30) and (32) we have some freedom to choose the main parameters of the models. Namely, p_{CH} and T_{CH} (satisfying $p_{CH}/p_C < T_{CH}/T_C$) for the CH model and p_{AR} and T_{AR} (satisfying $p_{AR}/p_C > T_{AR}/T_C$) for the AR model. Modifying these parameters affects the density values and eventually the magnetic field structure due to the coupling between the plasma and the magnetic field. We have an infinite number of possible solutions.

It is indispensable to remark that the assumed functional dependencies for pressure and temperature for both the CH and the AR are essentially the same. Equations (30) and (32) have the same dependence with the flux function A (but A is dissimilar for each structure) and the differences rely in the constant factors. But for the CH model, the multiplicative factor is always positive ($p_C - p_{CH} > 0$) and the same applies to the AR model ($p_{AR} - p_C > 0$). This suggests that although the two structures may seem to have very unlike physical properties, they can be described using a common picture. Thus, the nature of CH and AR is not so antagonistic according to our uninvolved representation. In this regard, one could compose a magnetic configuration containing both a CH and an AR, like the ones shown in Fig. 6, and the common thermal structure described by Eqs. (30) or (32) would produce depletions/enhancements in the density and temperature of the CH/AR contained in the system. This approach can be applied, for example, to investigate the coupling between CHs and ARs, but this topic is beyond the scope of the present work.

4.2. An approximate semi-analytical method to compute equilibria in the low–β regime

Once we have chosen the specific profiles for $p_0(A)$ and $T(A, z)$ the Grad-Shafranov equation needs to be solved to understand how the topology of the magnetic field changes according to the values of the plasma parameters. In general, finding solutions to Eq. (7) requires numerical methods unless that the profile for $p(A, z)$ and the boundary conditions are simple. It is known that only in the case that Eq. (7) is a linear equation general analytical methods are available. In the past a significant effort has been devoted to find exact analytical solutions in similar problems because they provide deep insights on the physics of the problem (see for example the extensive literature on the subject of B. C. Low). Before solving Eq. (7) by purely numerical means in Sect. 4.3 we introduce a semi-analytical method based precisely on the linearization of this equation. First, the nonlinear elliptic equation for the flux function is rewritten as

$$\frac{\partial^2 A}{\partial x^2} + \frac{\partial^2 A}{\partial z^2} + \epsilon f(A) = 0. \tag{34}$$

The parameter ϵ can be viewed as the plasma-β (see the equivalent nondimensional Eq. (9)) and $f(A)$ is the derivative of the pressure term with respect to A, given by Eq. (28) for the isothermal case or Eq. (28) modified according to Eq. (29) for the non-isothermal case.

To make analytical progress we use a pertubational expansion and write

$$A = A_0 + \epsilon A_1 + \epsilon^2 A_2 + ... \tag{35}$$

We obtain the following equation to zero order in ϵ

$$\frac{\partial^2 A_0}{\partial x^2} + \frac{\partial^2 A_0}{\partial z^2} = 0, \tag{36}$$

which is strictly the Laplace equation for A_0 that has been solved analytically in Sect. 3.2 given a superposition of parabolic magnetic field profiles at $z = 0$. The solution to this equation is just the potential magnetic field.

Now we apply a Taylor expansion to $f(A)$ keeping terms up to first order in ϵ,

$$f(A) \approx f(A_0 + \epsilon A_1) \approx f(A_0) + \epsilon A_1 f'(A_0) \tag{37}$$

Using this expansion in Eq. (34) we find, to first order in ϵ, the following equation

$$\frac{\partial^2 A_1}{\partial x^2} + \frac{\partial^2 A_1}{\partial z^2} = -f(A_0). \tag{38}$$

Equation (38) is just a Poisson equation for A_1 and the inhomogeneous or source term on the right hand side depends on the solution A_0 to the Laplace equation. Appropriate boundary conditions need to be applied, but the inhomogeneous BC at $z = 0$ has been incorporated to the Laplace solution and therefore homogeneous BCs (i.e., $A_1 = 0$) need to be imposed on the Poisson solution in order to have the full solution given by Eq. (35) satisfying the required BC at $z = 0$. Hence, so far the highly nonlinear problem has been reduced to solving a linear Laplace equation plus a Poisson equation which is also linear. Note that we can keep higher order terms in ϵ, to second order we have

$$\frac{\partial^2 A_2}{\partial x^2} + \frac{\partial^2 A_2}{\partial z^2} = -A_1 f'(A_0), \tag{39}$$

obtaining again a Poisson equation but the source term depends on A_1, and A_0, i.e., the previous order solutions. Nevertheless in this work we only consider terms up to first order in ϵ.

The method of images used to solve the Laplace equation in Sect. 3.2 is also applied here to solve the Poisson equation given by Eq. (38) but forcing the Green's function to be zero at $z = 0$ because of the required homogenous BC. In such a situation we have to use a source image of the point (x, z) with respect to the $x-$axis, $(x, -z)$. The analytical solution to the Poisson equation in this case is known to be (e.g. Myint-U & Debnath 2009)

$$A_1(x, z) = -\frac{1}{4\pi}\int_0^\infty \int_{-\infty}^\infty f(A_0(\xi, \eta)) \ln \frac{(x-\xi)^2 + (z-\eta)^2}{(x-\xi)^2 + (z+\eta)^2}\, d\xi\, d\eta. \tag{40}$$

This formal solution to the Poisson equation involves the evaluation of a double integral and in general it is rather difficult to obtain a closed analytical form of the solution in terms of known functions.

A purely numerical evaluation of Eq. (40) is required for the examples investigated in the present paper, for this reason we

provide the main steps to evaluate Eq. (40) numerically without major difficulties. First, we use the following result for the inner integral $\int_{-\infty}^{\infty} \mathcal{F}(y)\,dy = \int_{0}^{\infty} [\mathcal{F}(y) + \mathcal{F}(-y)]\,dy$. Then we introduce a variable transformation to have finite limits in the inner and outer integrals. A convenient variable transformation is $\xi = (1-t)/t$ and $\eta = (1-s)/s$ which changes the integration domain from $0 < \xi < \infty$ and $0 < \eta < \infty$ to the more convenient range $0 < s < 1$ and $0 < t < 1$. The double integral in terms of the new variables reads

$$A_1(x,z) = -\frac{1}{4\pi}\int_0^1\int_0^1 \left[f\left(A_0\left(\frac{1-t}{t},\frac{1-s}{s}\right)\right) \ln \frac{\left(x-\frac{1-t}{t}\right)^2+\left(z-\frac{1-s}{s}\right)^2}{\left(x-\frac{1-t}{t}\right)^2+\left(z+\frac{1-s}{s}\right)^2} + f\left(A_0\left(\frac{-1+t}{t},\frac{1-s}{s}\right)\right) \ln \frac{\left(x-\frac{-1+t}{t}\right)^2+\left(z-\frac{1-s}{s}\right)^2}{\left(x-\frac{-1+t}{t}\right)^2+\left(z+\frac{1-s}{s}\right)^2} \right] \frac{1}{t^2}dt\frac{1}{s^2}\,ds. \tag{41}$$

An examination of this double integral reveals that the points $t = 0$ and $s = 0$ need a special treatment in order to avoid (regular) singularities. This is accomplished by choosing a quadrature formula based on an open method that does not explicitly use the end points (located at 0 and 1 in our case, but 1 is not problematic) to calculate the integral. Trapezoidal and Simpson methods do not fall into this category but the standard composite midpoint method of integration is suitable. We find that this last method, with typically 200×200 points, is enough to provide accurate values of the integral and convergence of the results is warrantied.

Summarizing, the procedure to incorporate the effect of gas pressure and gravity in the model is: (a) calculate the potential solution A_0 (see Sect. 3.2), (b) build the function $f(A_0)$, (c) calculate A_1 using Eq. (41), (d) the final flux function is $A_0 + \epsilon A_1$, where $\epsilon = \beta_0/2$ (when dimensionless variables are used). This method is applied in the following to assemble a variety of models. In Fig. 7 we find a constructed model for an isothermal CH (no temperature variation along the magnetic field lines but temperature changes from line to line) in a low β situation. For the gas and temperature we use the dependence proposed in Eq. (30). We find that the plasma density is low inside the CH and grows gradually as we move towards the coronal environment. The effect of a finite pressure and gravity changes the expansion of the magnetic field (compare solid and dashed blue lines). The magnetic field lines get closer to each other in comparison with the potential magnetic field. The reason is that magnetic pressure increases to compensate the decrease of gas pressure inside the CH and to keep the balance in the total pressure. Temperature shows a depletion inside the CH and connects smoothly with the coronal environment. Since in this case temperature only depends on the flux function temperature isocontours match perfectly with the magnetic field lines but this is not true for the density distribution. The density contrast at the center of the CH and at $z = 0$ is $\rho_{\rm CH}/\rho_{\rm C} = (p_{\rm CH}/p_{\rm C})(T_{\rm C}/T_{\rm CH}) = 0.3125$ according to the pressure and temperature ratios of this example (given in the caption of Fig. 7). Since gas pressure and magnetic field change with position in the CH model, the plasma-β is a spatially dependent function. Different cuts of this dimensionless parameter at several positions are plotted in Fig. 8. Now we prefer to use 1D plots to facilitate the comparison with the fully numerical results described in the following section. From Fig. 8 we find that the plasma$-\beta$ attains its minimum values at the center of the CH ($x = 0$) where it is always below 0.05. As we move

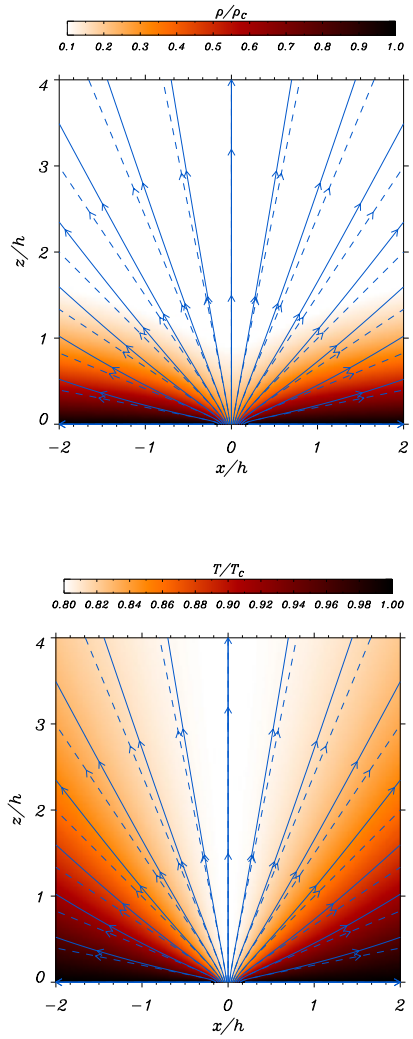

Fig. 7. Density and temperature distribution for the CH model with $\beta_0 = 0.004$. In this solution $p_{\rm CH}/p_{\rm C} = 1/4$, $T_{\rm CH}/T_{\rm C} = 0.8$, $x_0/h = 0.2$. The isothermal condition (along the field lines) is imposed in this model. The blue solid lines represent the magnetic field while the dashed lines correspond to the potential magnetic field. The footpoints of the two ensembles of magnetic field lines are exactly the same and a direct comparison is meaningful.

sideways from the center this parameter rises, being the increment especially significant at low heights. Near the position at $x/h = 2$ its value is around 6 (not shown in the figure). However, the behaviour with height of β approaches to the that found at $x/h = 0$ and therefore it has low values.

The situation with a temperature profile imposed to change with height according to Eq. (26) is displayed in Fig. 9. Under these conditions we find that density and the magnetic field are very similar to the previous case being the main difference the 2D temperature distribution (and gas pressure, not shown here) in the structure. The coronal plasma surrounding the central part of the CH reaches coronal temperatures while the lowest temperatures are found at low heights and inside the hole. Hence, in these two examples although the density distribution is very similar, we obtain that the thermal structure of the CH model can be rather different. In any case, the specific choice given by Eq. (30) provides a fairly realistic representation of typical CH

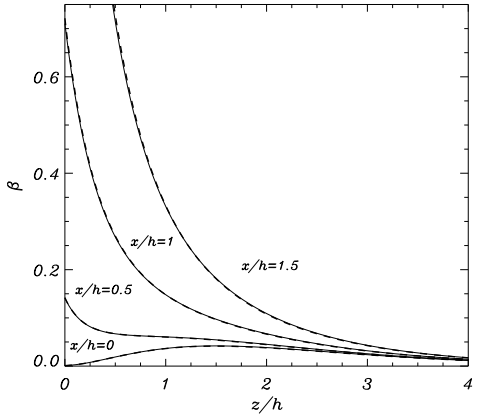

Fig. 8. Plasma-β as a function of height for the CH model with $\beta_0 = 0.004$ at different values of x (see the labels in the plot). The same parameters as in Fig. 7 have been used. The thin continuous lines correspond to the results based on the semi-analytical approach while the thick dashed lines represent the purely numerical results calculated using the code PDE2D described in Sect. 4.3. The agreement between the semi-analytical and the numerical curves is quite significant.

conditions. It is worth mentioning that the density contrast at the center of the CH and at $z = 0$ is the same as in Fig. 7 since precisely at $z = 0$ the two models have the same temperature and pressure values.

At this point and according to the results shown in Figs. 7 and 9 it is necessary to remark that the magnetic field topology and the density structure of the CH do not coincide. This has important implications regarding the setup and interpretation of MHD simulations of CHs but also for the interpretation of the observations of CHs and the possible location of the CHB. Nevertheless, our model does not provide information about plumes and rays in coronal holes which are nearly radially aligned density striations that are thought to follow the ambient magnetic field.

We now concentrate on ARs and compose several equilibrium models using the same semi-analytical procedure and the functional dependencies given by Eq. (32). Figure 10 shows the configuration that we obtain when $\mathcal{H}(z) = 1$. Density is strongly localized at the core of the AR and gravity produces the stratification effect visible outside the core. The magnetic field lines show a much stronger expansion in comparison with the potential case essentially produced by the high density and high pressure core. In this case magnetic pressure has to decrease to balance the excess of gas pressure at the core, and this produces a strong separation of the field lines when compared to the potential case. Temperature is also high at the core, reaching 4 MK, in comparison with the coronal temperature at 1 MK. These two temperatures are imposed in the model through the parameters $T_{\rm AR}$ and $T_{\rm C}$. The density contrast at the center of the AR and at $z = 0$ is $\rho_{\rm AR}/\rho_{\rm C} = (p_{\rm AR}/p_{\rm C})(T_{\rm C}/T_{\rm AR}) = 10$ using the pressure and temperature ratios of the model (given in the caption of Fig. 10).

The situation with a temperature increasing with height, $\Lambda = 20h$, is shown in Fig. 11. The density distribution is similar to the previous case and the main differences are in the temperature distribution which is higher in the plasma surrounding the core. In this configuration since temperature changes along the field lines the thermal conduction has an effect, discussed in Sect. 5. The temperature dependence with height has some influence on the structure of the magnetic field too (compare with Fig. 10).

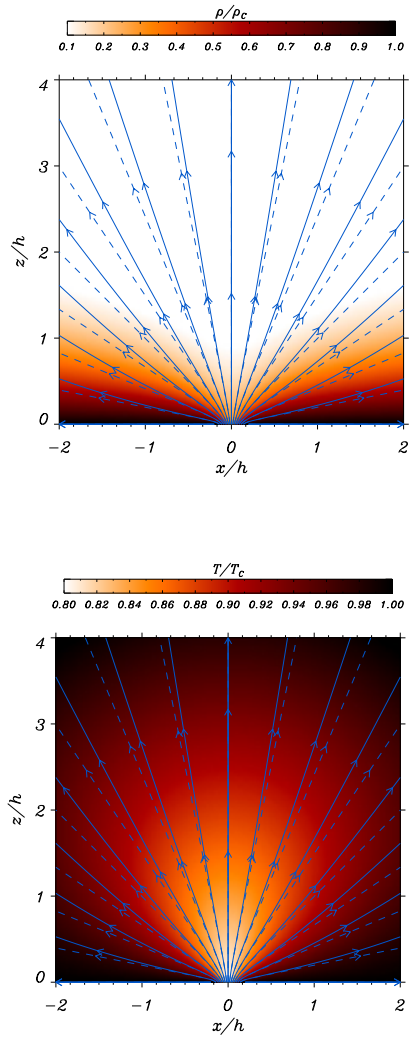

Fig. 9. Density and temperature distribution for the CH model with $\beta_0 = 0.004$. In this solution $p_{\rm CH}/p_{\rm C} = 1/4$, $T_{\rm CH}/T_{\rm C} = 0.8$, $x_0/h = 0.2$. Temperature is forced to increase with height with a moderate scale height variation, $\Lambda = 20h$. The blue solid lines represent the magnetic field while the dashed lines correspond to the potential magnetic field.

Equation (32) provides a route to build AR models with similarities with the diffuse background of bipolar regions reported in the observations. The structure of individual loops commonly found in real ARs is missing in our model, and considered as secondary for our purposes.

4.3. Numerical calculation of the equilibria in the low-β regime

When the plasma-β is not small the previous semi-analytical method to find a solution in not fully justified. In this case it is convenient to solve Eq. (7) by numerical means. Even in the low-β regime it is useful to have an alternative method to compare with the results of Sect. 4.2. We use the numerical code PDE2D (Sewell 2018) which solves, using finite elements, partial differential equations of the type found in our problem. We chose a collocation method with bicubic Hermite basis functions. This choice of basis functions ensures that the first derivatives of the approximate solution are all continuous. Newton's

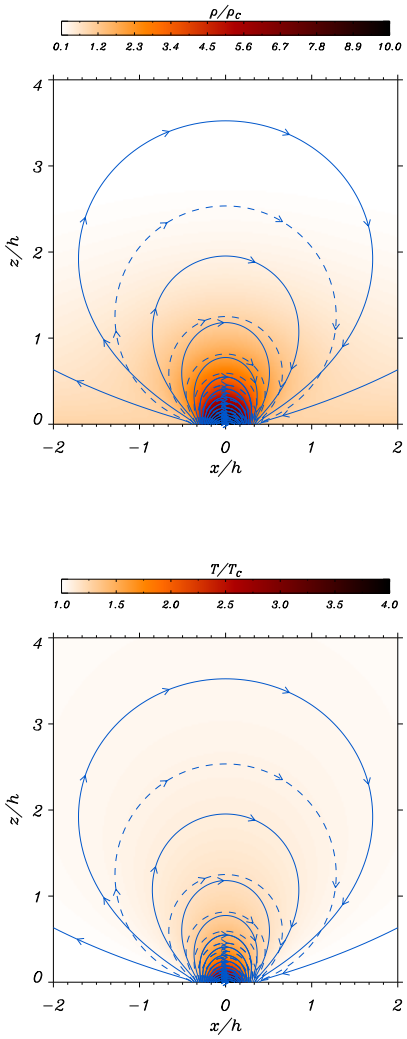

Fig. 10. Density and temperature distribution for the AR model with $\beta_0 = 0.004$. In this solution $p_{\rm AR}/p_{\rm C} = 40$, $T_{\rm AR}/T_{\rm C} = 4$, $x_0/h = 0.2$, $x_1/h = -1/4$, $x_2/h = 1/4$. The isothermal condition (along the field lines) is imposed in this model. The blue solid lines represent the magnetic field while the dashed lines correspond to the potential magnetic field.

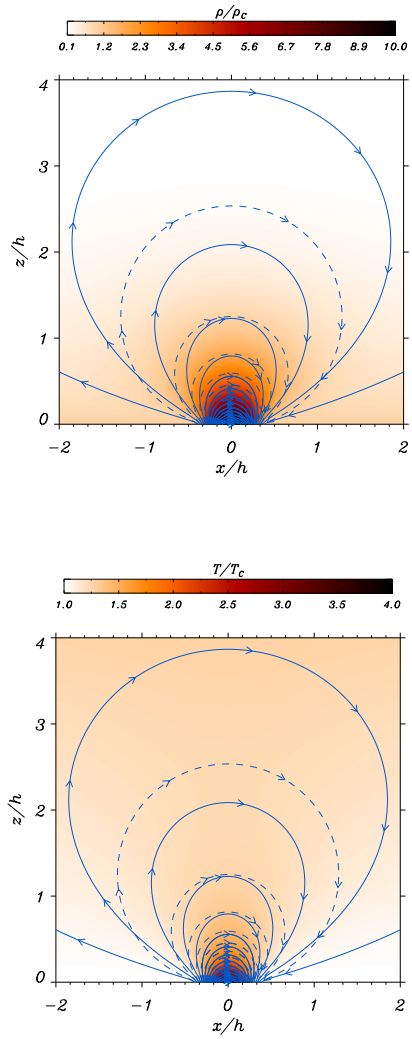

Fig. 11. Density and temperature distribution for the AR model with $\beta_0 = 0.004$. In this solution $p_{\rm AR}/p_{\rm C} = 40$, $T_{\rm AR}/T_{\rm C} = 4$, $x_0/h = 0.2$, $x_1/h = -1/4$, $x_2/h = 1/4$. Temperature is forced to increase with height with a moderate scale height variation, $\Lambda = 20h$.

method is used to iteratively solve the nonlinear algebraic equations resulting from the collocation method. Convergence is in general achieved in just four or five iterations when a given constant value as the initial guess of the solution in the whole numerical spatial domain is chosen (see Pizzo 1986, for another alternative numerical technique).

The particular choice of boundary conditions discussed earlier is also introduced into the numerical scheme and constitute an essential part of the problem. We aim at minimizing the effect of the lateral and upper boundaries on the solution and as we have shown a convenient approach is to impose the BC at infinity, except at $z = 0$ where we select the particular profile for the vertical component of the magnetic field. This is achieved by choosing a suitable coordinate system. In the $z-$direction we use the following transformation, sometimes referred as a Möbius transformation,

$$Z = \frac{1}{z/L_z + 1}, \tag{42}$$

and the initial domain $0 < z < \infty$ changes to $0 < Z < 1$ which is bounded. There is some freedom to chose the factor L_z in the transformation. In the $x-$direction we can chose an equivalent transformation if the system is symmetric with respect to $x = 0$, nevertheless we prefer not to be restricted to this situation. For this reason our choice is

$$X = \tanh\left(x/L_x\right), \tag{43}$$

and therefore instead of solving the problem in the range $-\infty < x < \infty$ with the new coordinate we just need to consider the interval $-1 < X < 1$. Again L_x is a factor that we have to select.

With the previous coordinate transformations we rewrite the 2D Laplacian in terms of the new coordinates by using the cor-

responding scale factors obtaining

$$\frac{\partial^2 A}{\partial x^2}+\frac{\partial^2 A}{\partial z^2}=\frac{1-X^2}{L_x^2}\left(-2X\frac{\partial A}{\partial X}+(1-X^2)\frac{\partial^2 A}{\partial X^2}\right)+\frac{Z^2}{L_z^2}\left(2Z\frac{\partial A}{\partial Z}+Z^2\frac{\partial^2 A}{\partial Z^2}\right). \quad (44)$$

Due to the coordinate transformation first order derivatives of A are present now. This equation plus the pressure term, given by Eqs. (28) and (29), is implemented in the numerical code PDE2D for the specific functions defined in Eqs. (30) or (32). Once we obtain a solution in the coordinates X and Z we perform a mapping to Cartesian coordinates for a better visualization of the results. The obtained solution in Cartesian coordinates must be independent of the factors L_x and L_z used in the transformation. This provides clues about the optimal choice of these parameters since in essence they control the spacing of the nonuniform grid viewed in Cartesian coordinates. For example, for the active region model the parameter L_x must be of the order of the separation of the two unipolar regions, $2x_1$.

The numerical results for exactly the same situation as in Fig. 7 (calculated using the semi-analytical approach) have been computed numerically using a grid of 200×200 points. A comparison of the plasma-β using the two methods is available in Fig. 8. This figure demonstrates that the two results are almost identical and the differences appear when the plasma$-\beta$ rises. This corroborates that the semi-analytical method is accurate enough to be used as a tool to formulate equilibria in the low-β regime. Adding second other terms to the semi-analytical approach would increase further the accuracy of the method.

Another procedure to check that the semi-analytical and/or the numerical solutions are correct, is to introduce the obtained profile for $A(x, z)$ and the corresponding pressure and density distributions in Eq. (7) and to compute the force balance. For the purely numerical results we find that as the resolution is increased the force balance converges towards zero indicating that our numerical solutions are truthful representations of the real solution to Eq. (7). Nevertheless, we have found that as the plasma-β rises (typically for $\beta_0 = 0.1$), the numerical solution is not as accurate and convergence issues appear. These issues are not mitigated when the spatial resolution is increased and are more likely related to the intrinsic nature of the nonlinear terms.

5. Energy balance

In Sect. 4.2 we have obtained magnetohysdrostatic solutions under a balance between the Lorenz force, the pressure gradient and the gravity force. Apart from the force equilibrium the system should also satisfy energy balance. Obviously, if we consider that we are in ideal MHD the response is trivial since the effects of thermal conduction, radiative losses and heating are ignored. In this case the equilibrium solutions derived in the previous sections under force balance can be used, together with an adiabatic energy equation, to study different processes, for example, the temporal evolution of MHD waves in the system. A possible application of the models developed in the present work is the analysis of the evolution of global MHD waves interacting with CH or AR since in this problem the assumption of ideal MHD is justified as a first step if the focus is on the properties of the waves.

In reality the assumption of ideal MHD in the solar corona is a poor approximation since thermal conduction, optically thin radiation and heating are processes that can not be ignored in general (it depends on the temporal scales we are interested in). We need to address how these effects are included in our models. The question is in fact simple and clearly explained in Low (1975, 1980), the energy equilibrium (or thermal balance) can be calculated only "a posteriori" in the scheme used in this paper. Once we have the force balanced solution, i.e., the temperature and density distribution in 2D, we can calculate the conduction term, E_C, and the radiation term, E_R, according to their expressions and then derive the distribution of the heating term, H, to have a perfect energy balance. In this situation we are deriving from the model the heating distribution using the following equation

$$H(x, z) = E_C(x, z) + E_R(x, z). \quad (45)$$

Note that using this procedure we are not calculating self-consistently the temperature distribution according to a known energy equation. This can only be achieved, and this point is relevant, assuming an "ad hoc" explicit dependence of the heating function with, for example, the density, temperature or magnetic field. But the exact form of the heating function and its source is precisely one of the main unknowns in relation to the coronal heating problem. Nevertheless, we think that deriving the heating distribution once we obtain a force balance for a prescribed temperature and pressure profiles is an approach that is worth to be investigated. Somehow the available energy in the system is constrained by the requirement of force balance. It does not necessarily mean that the obtained heating function using this method is closely related to the real heating source in the solar corona, but it still can provide useful information about the energetics of system. In the following we try to make this point clearer. As far as we know, this distinctive approach has not been explored in the literature, at least in the form proposed here in relation to the two-dimensional problem.

We start with the most elementary situation, the model of constant temperature along the magnetic field lines. Temperature can change from line to line though, due the dependence $\mathcal{T}(A)$. Thermal conduction is zero under this assumption (we do not consider conduction perpendicular to the magnetic field). This means that the only possibility to have thermal equilibrium is that the heating has to balance exactly the radiative losses. This is a rather unlikely situation from the physical point of view, but it has been suggested by Aschwanden et al. (1999, 2000) since their observations indicate that coronal loops of different active regions are essentially in an isothermal state, and therefore thermal conduction is essentially zero. Nevertheless, the focus of our work is not in coronal loops but in the diffuse background, which does not necessarily need to have the same isothermal character.

Thermal conduction has an effect in our model if we consider that temperature has also a dependence with height, i.e., $T(A, z)$. We know that the thermal conduction term in the energy equation (see for example Priest 1982) can be expressed as

$$E_C = \nabla \cdot \mathbf{q} = -\nabla \cdot \left(\kappa_\parallel \left(\nabla T \cdot \hat{\mathbf{B}}\right)\hat{\mathbf{B}}\right), \quad (46)$$

which is written here in terms of the unitary magnetic field vector $\hat{\mathbf{B}} = \mathbf{B}/B$. The heat flux is represented by $\mathbf{q}$ and it is parallel to the magnetic field (assuming that $\kappa_\perp = 0$, as mentioned earlier). Using vector identities and the fact that $\nabla \cdot \mathbf{B} = 0$ the previous expression reduces to

$$E_C = -\mathbf{B} \cdot \nabla\left(\frac{\kappa_\parallel}{B^2}(\nabla T \cdot \mathbf{B})\right) = -\frac{d}{dl}\left(\kappa_\parallel \frac{dT}{dl}\right) + \frac{\kappa_\parallel}{B}\frac{dB}{dl}\frac{dT}{dl}, \quad (47)$$

where on the right hand side we have used the coordinate l along the magnetic field $\mathbf{B}$. Thermal conduction has two contributions, related to the variation of temperature along the field lines and also due to changes in the modulus of the magnetic field along l or equivalently to the change in area of the corresponding flux tube. The conduction term, $E_{\rm C}$, can be either positive or negative and depends on the location in the domain, hence it is a spatially-dependent function.

Using the separable form for the assumed temperature dependence in this work, Eq. (24), we evaluate the factors in the heat flux definition finding that

$$\nabla T \cdot \mathbf{B} = \frac{\partial T}{\partial x} B_x + \frac{\partial T}{\partial z} B_z = \frac{\partial \mathcal{T}}{\partial A} B_z B_x \mathcal{H} - \frac{\partial \mathcal{T}}{\partial A} B_x B_z \mathcal{H} + \mathcal{T} B_z \frac{d\mathcal{H}}{dz} = \mathcal{T} B_z \frac{d\mathcal{H}}{dz}, \tag{48}$$

where we have used the chain rule and the definition of the magnetic field components in terms of the flux function A. Using the previous expression and the fact that $\kappa_{\parallel} = \kappa_0 T^{5/2}$ ($\kappa_0 = 1.1 \times 10^{-11}$ W m^{-1} K$^{-7/2}$), the heat flux vector reads

$$\mathbf{q} = -\kappa_0 \mathcal{T}^{7/2} \frac{B_z}{B^2} \frac{d\mathcal{H}}{dz} \mathcal{H}^{5/2} \mathbf{B}. \tag{49}$$

For the explicit exponential dependence of the function $\mathcal{H}(z)$ given by Eq. (26) we obtain that the vertical component of the heat flux vector is

$$q_z = \mathbf{q} \cdot \hat{\mathbf{e}}_{\mathbf{z}} = -\kappa_0 \mathcal{T}^{7/2} \frac{B_z^2}{B^2} e^{(7/2)\, z/\Lambda} \frac{1}{\Lambda}. \tag{50}$$

When temperature is independent of z the parameter Λ tends to infinity and the heat flux is zero since we are in the isothermal situation along each field line. Equation (50) indicates that a finite Λ introduces a net heat flux in the vertical direction. At the bottom layer of the domain ($z = 0$) we have an incoming vertical heat flux for negative Λ while it is outgoing for positive Λ. This has a relevant effect since heat, coming from below our reference level for positive Λ, modifies the thermal balance of the system. The opposite situation, i.e., heat leaving the system through the bottom boundary is only possible if temperature increases with height. Note that the vertical heat flux is independent of the sign of B_z according to Eq. (50).

The horizontal heat flux is

$$q_x = \mathbf{q} \cdot \hat{\mathbf{e}}_{\mathbf{x}} = -\kappa_0 \mathcal{T}^{7/2} \frac{B_z B_x}{B^2} e^{(7/2)\, z/\Lambda} \frac{1}{\Lambda}. \tag{51}$$

Contrary to the vertical component, the horizontal component of the heat flux depends on the signs of B_z and B_x and this is a consequence of the fact that the heat flux vector is pointing along the magnetic field. Only in the situation of a purely vertical magnetic field (the center of a symmetric CH) or a purely horizontal magnetic field (the center of a symmetric AR) the horizontal heat flux is zero. It is worth mentioning that even in the situation of zero heat flux, thermal conduction can be different from zero (since this magnitude is the divergence of the heat flux, Eq. (46)).

From the previous expressions it is easy to obtain the explicit form of the energy conduction when the magnetic field is purely vertical or purely horizontal. For the purely vertical magnetic field at the center of the CH we find (see Eq. (47)) that

$$E_{\rm C}(x = 0, z) = -\frac{\partial}{\partial z} \left(\kappa_0 \mathcal{T}^{7/2} \frac{d\mathcal{H}}{dz} \mathcal{H}^{5/2} \right) + \kappa_0 \mathcal{T}^{7/2} \frac{d\mathcal{H}}{dz} \mathcal{H}^{5/2} \frac{\partial |B_z|}{\partial z} \frac{1}{|B_z|}. \tag{52}$$

This expression applied to the exponential dependence with height of temperature reduces to

$$E_{\rm C}(x = 0, z) = \kappa_0 \mathcal{T}^{7/2} e^{(7/2)\, z/\Lambda} \frac{1}{\Lambda} \left(-\frac{7}{2} \frac{1}{\Lambda} + \frac{\partial |B_z|}{\partial z} \frac{1}{|B_z|} \right). \tag{53}$$

For the CH model used in the present work we have that $\partial |B_z| / \partial z < 0$ at $x = 0$, independently of z. This means that for $\Lambda > 0$ we always obtain that $E_{\rm C}(x = 0, z) < 0$ according to Eq. (53). But for $\Lambda < 0$ the sign of energy conduction can change depending on the terms inside the parenthesis. In particular when

$$\frac{7}{2} \frac{1}{|\Lambda|} < \left| \frac{\partial |B_z|}{\partial z} \right| \frac{1}{|B_z|}, \tag{54}$$

then $E_{\rm C}(x = 0, z) > 0$. Nevertheless, this condition might be only satisfied up to a certain height, as we show later.

For a purely horizontal magnetic field, taking place at the center of the symmetric AR model, it is possible to perform a similar analysis as for the CH at $x = 0$. In this case it is not difficult to show that

$$E_{\rm C}(x = 0, z) = -\kappa_0 \mathcal{T}^{7/2} e^{(7/2)\, z/\Lambda} \frac{1}{\Lambda} \frac{\partial B_z}{\partial x} \frac{1}{B_x}, \tag{55}$$

which is different to Eq. (53). Since the magnetic configuration of the AR has a concave geometry at $x = 0$ then $(\partial B_z / \partial x)/B_x < 0$. Hence, for $\Lambda > 0$ Eq. (55) indicates that we always obtain that $E_{\rm C}(x = 0, z) > 0$, while for $\Lambda < 0$ we have the opposite situation, $E_{\rm C}(x = 0, z) < 0$. These characteristics of the sign of the conduction term have important consequences regarding the energy balance.

We turn our attention to the radiative losses. Since we are considering coronal plasmas we use the optically thin losses of Hildner (1974) for simplicity, other functions can be used though (see Athay 1986, Dere et al. 1997, Klimchuk & Cargill 2001, and Landi et al. 2012). As usual $E_{\rm R} = \rho^2 Q(T)$, where $Q(T)$ is the corresponding loss function depending only on temperature. From the force balance equation we obtain the density and the temperature distribution in 2D, and this information is used to compute the spatial distribution of the 2D radiative losses using the previous expression. Once we know the radiative losses and the conduction term, it is straight forward to calculate, using Eq. (45), the spatial distribution of the heating to have energy balance. Based on physical grounds the heating must be positive, representing a source of energy that needs to be supplied to the system to have energy balance. Nevertheless, in our approach it may happen that in some regions of the 2D configuration the condition of positiveness is not satisfied. The reason relies in the fact that, as we have shown before, the conduction term is either positive or negative, while the radiation term is always positive. The sum of these two terms is not necessarily a positive number. In this case the obtained heating is negative and represents a non-physical energy sink. The system can not achieve energy balance in this situation. We demonstrate this behaviour by calculating the different terms in the energy equation for several of the models presented earlier. The results for a CH are shown in Fig. 12. The conduction term is negative in most of the domain and typically one order of magnitude smaller that the radiation term. In particular, we have shown that for the vertical magnetic field line at the center of the CH the conduction term is always negative when temperature increases with height (the present example). In this situation the sum of radiation and conduction is positive up to one scale height at $x = 0$. The dashed line in the plot for the heating H, represents the curve that separates the transition

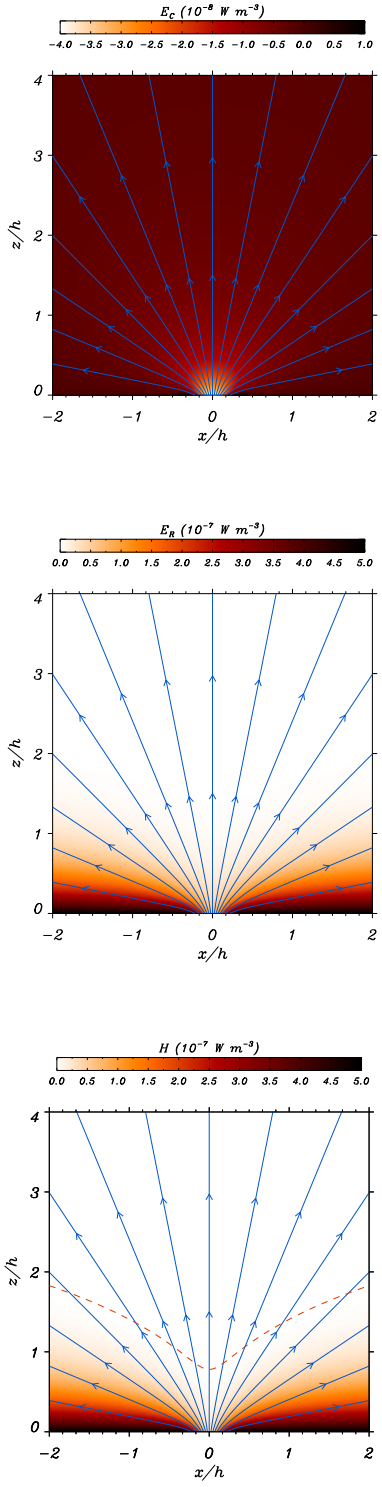

Fig. 12. Conduction, radiation and heating terms for the CH model. The boundary marked with dashed lines in the heating term separates the transition from energy balance to non-energy balance (energy balance below the curve, non-energy balance above the curve). In this plot $\Lambda = 200h$. In the present model the reference values are $\rho_0 = 5{\times}10^{-13}$kg m^{-3} and $T_0 = 1$ MK.

between the energy balanced and non-energy balanced points of the domain. At low heights, typically below $z = h$, the heating has to balance the radiation losses, and it has a rather reduced value inside the coronal hole, where density and temperature are lower than in the environment. In this example, the gradient of temperature with height is quite weak, since $\Lambda = 200h$, but this has a relevant effect due to the profile of conduction term.

The location of the transition curve depends on the parameters as Fig. 13 indicates. For example, for $\Lambda = 20h$, no energy balance is possible inside the coronal hole even at $z = 0$.Therefore, this situation is difficult to achieve from the physical point of view. Nevertheless, when Λ rises, see $\Lambda = 200h$ and $400h$, the boundary moves progressively upward, meaning than in the range $0 < z < 1.5h$ at $x = 0$, energy balance is accomplished for $\Lambda = 400h$. A small vertical gradient in temperature has a significant effect on the overall energy balance in the system.

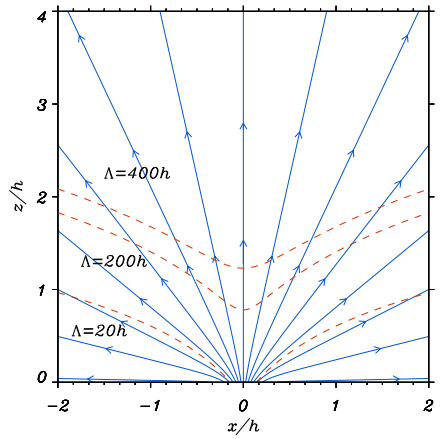

Fig. 13. Example of the location of the boundary, red dashed lines, that separate regions where energy balance is allowed (below these lines) from regions where it is not permitted (above the lines). In this case temperature increases with height ($\Lambda > 0$). The magnetic field is also displayed with blue lines

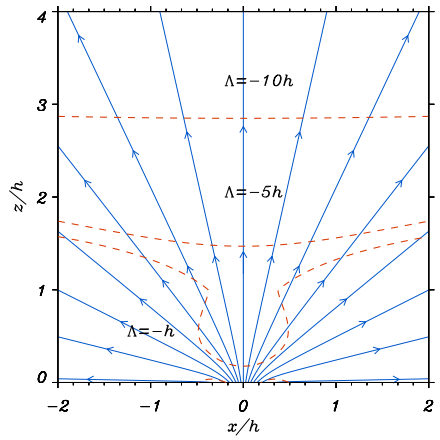

Fig. 14. Same as in Fig. 13 but temperature decreases with height ($\Lambda < 0$).

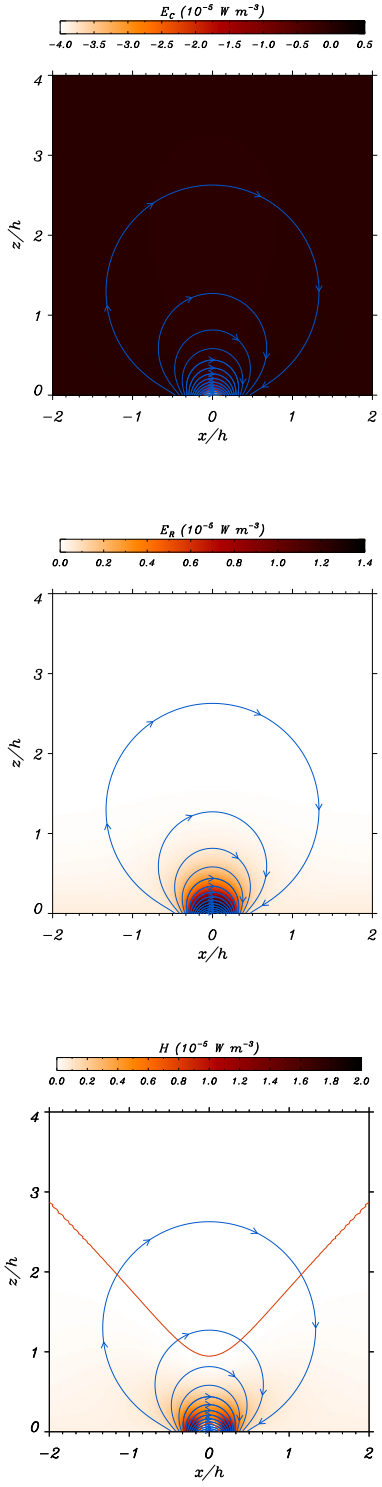

Fig. 15. Conduction, radiation and heating terms for the AR model. The boundary marked with a continuous line in the heating term separates the transition from energy balance to non-energy balance (energy balance below the curve, non-energy balance above the curve). In this plot $\Lambda = -20h$.

Figure 14 shows the same kind of plot as in Fig. 13 but for a decreasing temperature with height. We again find the presence of transitions between energy balanced and non-balanced situations. Interestingly, the corresponding curves do not show the strong dependence with the value of Λ found in Fig. 13. Only for values of Λ in the range from $-10h$ to $-h$ the curves are inside the limits of the domain of the plot. For the case $\Lambda = -h$ we find that, apart from the minimum located at $x = 0$ around $z = 0.25h$, there are two tiny additional symmetric zones of non-equilibrium at $z = 0$. These two zones are produced because conduction is negative and larger (in absolute value) than the radiative losses. For the rest of the curves the location of the height at $x = 0$ where we find non-equilibrium is closely related to the condition given by Eq. (53).

The same analysis is performed for the AR model. The different terms in the energy equation are plotted in the three panels of Fig. 15 for a temperature profile that decreases with height. The conduction term is quite low except at the core of the AR where it becomes negative. In fact it is always negative when the magnetic field is purely horizontal, as Eq. (55) indicates. When added to the radiation term the obtained heating distribution shows some forbidden zones represented with continuous red lines. Interestingly, the estimated heating is localized near the footpoints where the vertical component of the magnetic field is large and above the forbidden zone at the core of the AR.

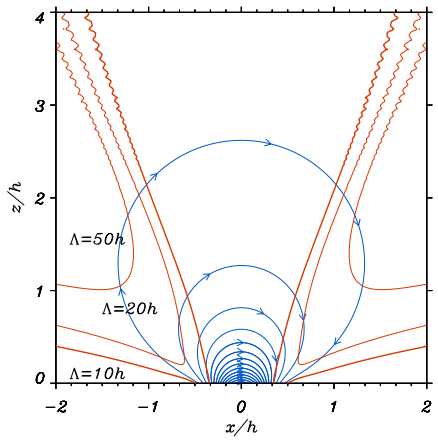

Fig. 16. Same as in Fig. 13 but for the AR model. Temperature increases with height ($\Lambda > 0$).

On the contrary, for a temperature that increases with height, see Fig. 16, the central part of the active region allows energy-balanced solutions since the conduction term is always positive at $x = 0$ according to Eq. (55). In this regard, low lying magnetic arches are the most suitable to be in energy balance for $\Lambda > 0$. However, when temperature decreases with height, see Fig. 17, the curves are similar to that in the CH model, except that very low lying curved fields situated at the core of the AR are now out of thermal equilibrium, as expected from the results shown in Fig. 15. These results demonstrate that small temperature gradients with height can have a significant effect on the energy equilibrium of the system, producing zones where balance can not be achieved. Along this line, we have explored different dependencies of the function $\mathcal{H}(z)$ that deviate from the simple exponential form of Eq. (26), and we have not been able to find a function that allows energy balance in the whole spatial domain. This result suggests that such global thermal balance is quite difficult to achieve in a real magnetic structure. Non-thermal equilibrium seems to be difficult to avoid and this might

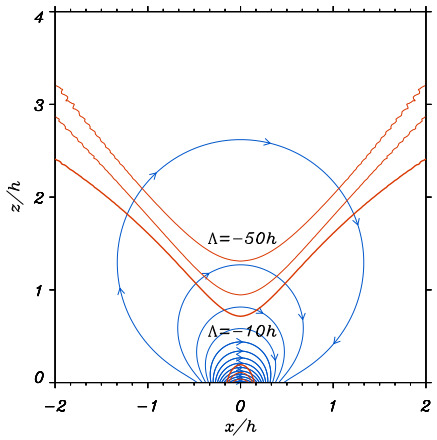

Fig. 17. Same as in Fig. 16 but now temperature decreases with height ($\Lambda < 0$). The situation shown in Fig. 15 is also represented here.

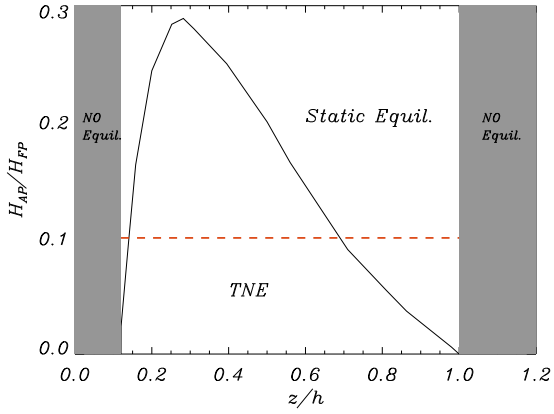

Fig. 18. Heating at the apex over the heating at the footpoint of a given field line as a function of height at $x = 0$ (continuous line). The results shown in Fig. 15 have been used to construct this plot, where the criteria of Klimchuk & Luna (2019) regarding TNE has been applied ($H_{AP}/H_{FP} < 0.1$ leads to TNE, represented with a horizontal red dashed line).

partially explain the occurrence of phenomena like coronal rain which is regularly observed (see for example Antolin & Rouppe van der Voort 2012 and Antolin 2020 and references therein). Nevertheless, very specific conditions are required for TNE to occur as we describe in the following.

Finally, it is worth analysing the possible occurrence of TNE in our system using known results regarding this process. Klimchuk & Luna (2019) have derived, using several approximations, some basic conditions that lead to the presence of TNE in coronal magnetic flux tubes. According to their results when the ratio of the heating at the apex of a given magnetic field line over the heating at the base of the corona on the same line (H_{AP}/H_{FP}) is smaller than 0.1, the system is prone to develop cycles associated to TNE. Asymmetries can alter the conditions for TNE (see also Pelouze et al. 2021) but they do not play any role in our perfectly symmetric configuration. We have calculated this ratio from the example shown in Fig. 15 using our computed heating (based on energy balance) and the results are represented in Fig. 18 as a function of the height of the different field lines at $x = 0$. There are two forbidden regions for heights below 0.1 and for heights above 1 (as Fig. 15 already shows) where equilibrium is not permitted. Close to these two regions we obtain values for the heating ratios below 0.1, meaning that the system would be in TNE according to the criteria of Klimchuk & Luna (2019). On the contrary, in the range of heights between $0.15 \leq z/h \leq 0.7$ the system would achieve a static equilibrium. Although our model does not include a chromosphere, which is an elementary ingredient to have TNE with periodic cycles, the calculated heating in our model can be used as a guide to infer the possible dynamical evolution of the system.

6. Conclusions and discussion

This study represents an exploratory first attempt at understanding the physics of coronal holes and active regions from a global point of view, instead of focusing on individual magnetic field lines. We have developed a rather flexible, robust methodology for generating two-dimensional magnetostatic equilibria in Cartesian geometry under the presence of constant gravity. We have artificially built a magnetic field distribution at the base of the corona based on the superposition of parabolic magnetic field profiles which have been translated in terms of the flux function, A. This function satisfies a Grad-Shafranov type of partial differential equation in 2D that contains a nonlinear term due to the coupling with gas pressure and temperature. The magnetic field arrangement, chosen to represent open and closed magnetic field lines, is incorporated through the boundary conditions needed to solve the partial differential equation. We have been able to find manageable analytical expressions for the magnetic distribution in the potential case.

Based on physical grounds and the information provided by observations, we have proposed a relatively simple functional form for plasma pressure and temperature in terms of the flux function. We have selected a depression in pressure and temperature inside the CH to have a realistic model. Under such conditions density is found to be lower inside the CH with respect to the coronal environment if the elementary constraint $p_{CH}/p_C < T_{CH}/T_C$ is satisfied. A decrease in gas pressure produces an increase in magnetic pressure in order to keep the total pressure constant across the field lines. Along the magnetic field lines there is, by construction in the model, balance between the gas pressure gradient and the projected gravitational term. On the contrary, in our ARs models the core is overdense when $p_{AR}/p_C > T_{AR}/T_C$. Interestingly, the same functional form of gas pressure and temperature with the flux function describes correctly the general features of both CHs (low pressure, temperature and density) and ARs (high pressure, temperature and density) which are in principle two considerably different coronal structures. We think that a compelling contribution of our model relies on the finding of solutions that can represent concurrently two different magnetic structures with properties similar to those reported by the observations. In this regard, it is imperative to mention that the exact dependence of pressure and temperature with the flux function A considered in the present work is not a crucial step of our analysis. Other choices can also lead to physically acceptable solutions.

The highly nonlinear term that couples the gas pressure effect to the magnetic field substantially complicates the derivation of analytical solutions. Nevertheless, the linearization of the Grad-Shafranov equation leads to a Poisson equation with a source term that depends on the potential solution that it is obtained from a Laplace equation. The formal solutions to these

two equations are written using Green's functions and applying the method of images. The outcome of the present study is a semi-analytical method, valid in the low β regime, that includes the effect of gas pressure and gravity. There are other alternatives that can be explored in the future to solve the characteristic nonlinear equation without assuming that the plasma-β is a small parameter, for example Liao (2003) for a novel method based on homotopy analysis. An interesting result obtained by applying our semi-analytic method is that in CHs the density distribution is not necessarily aligned with the magnetic field. Thus, the usual assumption that density structures delineate the magnetic field in the corona is not fully justified in open structures such as CHs.

The focus of this work has been on finding MHS solutions under force balance, and the possible energy balance has been calculated once the solution is known. We have shown by calculating the conduction and radiation terms that the corresponding heating necessary to maintain energy equilibrium is constrained in the spatial domain. The reader is also referred to the work of Petrie et al. (2003) where a similar approach was used but based on a fully analytic model. These authors where able to calculate models whose loop length, shape, plasma density, temperature and velocity profiles were fitted to loops observed with different satellites. In our model, depending on the parameters, especially the temperature dependence with height, it may occur that thermal balance can not be achieved at certain locations. Under these circumstances the system will most likely evolve either towards a different equilibrium configuration or develop cycles around a non existing equilibrium, such as happens in TNE processes. In the first case the excess of heat can be used to increase the temperature and gas pressure of the plasma along the field line. The evolution of the system strongly depends on the boundary conditions applied at the footpoints, and especially on the condition on the heat energy flux. The presence of a chromosphere at the footpoints also affects the evolution of the system, and it is especially relevant regarding TNE processes. The temporal evolution is a topic by its own and it is out of the scope of the present work, but the results presented here provide hints about the possible progression of the system with time. Note that since TNE is a non-linear mechanism the absence of equilibrium in a stationary configuration does not directly imply a TNE state. Recently several authors have carried a parameter space investigation (see Froment et al. 2018 and Pelouze et al. 2021) for TNE onset in a 1D geometry considering the possibility of asymmetric heating (along the loop) and asymmetric geometry. Besides TNE they also show the conditions in which steady or static state is achieved. Importantly, they found that when the heating is small (but typical of AR), TNE happens only when geometries and heating profiles match specific criteria. That is, at low energies, the TNE parameter space seems to be strongly constrained (see also Klimchuk & Luna 2019). As an illustrative example we have calculated the criteria for one of our models.

It is worth to remark that the main critical point of the approach used in this work regarding the energy balance is that the energy equation is not treated self-consistently. Nevertheless, the exact dependence of the heating function is required to solve the problem in a self-consistent manner. The heating function has several parametrizations depending on the heating mechanism invoked (e.g. Mandrini et al. 2000 and Démoulin et al. 2003), but the exact form of the heating function in the corona is still under debate. For this reason, we think that determining the heating function based on the constrains of force balance and thermal balance is an alternative path that should not be necessarily discarded. Although the condition of thermal or energy balance in the solar corona is not fully justified because some observations suggest the presence of low frequency nanoflare events in AR leading to non-steady heating, investigating the steady situation still provides useful information. In particular we have shown that if temperature has a monotonic dependence with height (either increasing or decreasing) then we obtain regions in the magnetic configuration where an appropriate amount of heating leads to a perfect energy balance. However, we also find regions where energy balance is not possible, and this depends on the scale of the temperature variation with height that eventually modifies the conduction and the radiative losses in the system. It might be worthy in the near future to compare the heating function we obtain from our models with those commonly used in the literature in order to assess the possible similarities/discrepancies among them.

We have used a magnetic unipolar configuration for the coronal hole. Although there are indications in the observations that the field is unipolar based on the estimations of the unsigned flux, the magnetograms show the typical salt and pepper distribution inside coronal holes. Our models only explain the upper part of the magnetic field in the solar corona where the magnetic field is essentially open (e.g. Wiegelmann & Solanki 2004). The models we have developed are fairly basic and very idealized, but contain the primitive ingredients to provide a common physical background that describes the elementary features of CHs and ARs. Nevertheless, we think that the previous assumptions are mandatory to make analytical progress and to understand the basic physical concepts that lie underneath this problem. The models developed here can be extended further. In particular, a stimulating extension of the present work is the analysis of MHS equilibria that contain both a CH and an AR separated by a certain distance. By analysing how the main parameters of one structure depend on the parameters of the other, may provide us information about the coupling between the two magnetic arrangements. This may pave a path to view CHs and ARs as connected structures.

In this work we have assumed that the temperature profile depends only on the magnetic field line (on the flux function A) and it has an explicit dependence on height in the coronal part of the atmosphere. Nevertheless, the model can be extended to include the lower parts of the solar atmosphere by choosing a temperature and pressure variation with height representative of the chromosphere, the transition region and finally the corona. In this future model the coupling of the corona with the chromosphere will be included and can have relevant effects on the coronal part of the solution, for this reason it deserves to be investigated further. The thermal balance under these conditions is also of interest but much more complicated because of the intricate physics of the solar chromosphere. For example, the radiative losses are no longer optically thin and therefore the loss functions used for the coronal part are not applicable. A chromospheric layer is known to act as a reservoir of energy and mass that can lead to the appearance of condensations in the corona and to cycles of thermal non equilibrium.

The present results should be also expanded to include flows. This is a more realistic situation than the static case since there are clear evidences in the observations of the presence of outgoing flows in coronal holes which are inevitably linked to the solar wind. To simplify things we should suppose first that the flow is field aligned. This problem has been investigated in the past by several authors in other contexts, see for example Tsinganos (1981, 1982), Low & Tsinganos (1986) and Webb et al. (1994, 2001), and in coronal loops by Petrie et al. (2002, 2003). Under the presence of flows there is a coupling between the Grad-Shafranov equation and the Bernoulli equation. This problem is

left for future studies and it is closely related to the appearance of TNE cycles also. TNE is due to the necessity of an enthalpy flux to balance energy loss in the corona. In the long run this is an unstable configuration due to the build-up of mass and runaway radiative losses.

Finally, the solutions obtained in the present work should be extended to the three-dimensional case which is more representative of a real situation. The coronal hole model can be translated to cylindrical geometry, while a different approach is required to represent bipolar active regions in 3D. The logical next step is to use Euler potentials although they have some limitations that need to be assessed depending on the specific configuration (see details in Neukirch 2015). Other "ad hoc" approaches to build analytic solutions in 3D that can be useful for our purposes have been investigated by Low (1985, 1991), Neukirch & Rastätter (1999), and Neukirch & Wiegelmann (2019), although a purely numerical treatment is most likely required in 3D when the thermal structure is included in the problem like in the present study.

Acknowledgements. This publication is part of the R+D+i project PID2020-112791GB-I00, financed by MCIN/AEI/10.13039/501100011033. M. L. acknowledges support through the Ramón y Cajal fellowship RYC2018-026129-I from the Spanish Ministry of Science and Innovation, the Spanish National Research Agency (Agencia Estatal de Investigación), the European Social Fund through Operational Program FSE 2014 of Employment, Education and Training and the Universitat de les Illes Balears. I. A. was supported by project PGC2018-102108-B-I00 from Ministerio de Ciencia, Innovación y Universidades and FEDER funds. P. A. acknowledges funding from his STFC Ernest Rutherford Fellowship (No. ST/R004285/2). The authors thank the referee, Prof. Tsinganos, for useful comments that helped to improve the paper.

References

Antolin, P. 2020, Plasma Physics and Controlled Fusion, 62, 014016
Antolin, P., & Rouppe van der Voort, L. 2012, ApJ, 745, 152
Aschwanden, M. J., Alexander, D., Hurlburt, N., et al. 2000, ApJ, 531, 1129
Aschwanden, M. J., Newmark, J. S., Delaboudinière, J.-P., et al. 1999, ApJ, 515, 842
Athay, R. G. 1986, ApJ, 308, 975
Cranmer, S. R. 2009, Living Reviews in Solar Physics, 6, 3
Del Zanna, G., & Mason, H. E. 2003, A&A, 406, 1089
Démoulin, P., van Driel-Gesztelyi, L., Mandrini, C. H., Klimchuk, J. A., & Harra, L. 2003, ApJ, 586, 592
Dere, K. P., Landi, E., Mason, H. E., Monsignori Fossi, B. C., & Young, P. R. 1997, A&ASup.Series, 125, 149
Downs, C., Roussev, I. I., van der Holst, B., et al. 2011, ApJ, 728, 2
Froment, C., Auchère, F., Mikić, Z., et al. 2018, ApJ, 855, 52
Gallagher, P. T., Phillips, K. J. H., Lee, J., Keenan, F. P., & Pinfield, D. J. 2001, ApJ, 558, 411
Golub, L., Maxson, C., Rosner, R., Vaiana, G. S., & Serio, S. 1980, ApJ, 238, 343
Hildner, E. 1974, Sol. Phys., 35, 123
Isenberg, P. A., & Vasquez, B. J. 2007, ApJ, 668, 546
Klimchuk, J. A. 2019, Sol. Phys., 294, 173
Klimchuk, J. A., & Cargill, P. J. 2001, ApJ, 553, 440
Klimchuk, J. A., & Luna, M. 2019, ApJ, 884, 68
Landi, E., Del Zanna, G., Young, P. R., Dere, K. P., & Mason, H. E. 2012, ApJ, 744, 99
Liao, S. 2003, Beyond Perturbation: Introduction to the Homotopy Analysis Method, Modern Mechanics and Mathematics (CRC Press)
Low, B. C. 1975, ApJ, 197, 251
—. 1980, Sol. Phys., 65, 147
—. 1985, ApJ, 293, 31
—. 1991, ApJ, 370, 427
Low, B. C., & Tsinganos, K. 1986, ApJ, 302, 163
Mandrini, C. H., Démoulin, P., & Klimchuk, J. A. 2000, ApJ, 530, 999
Munro, R. H., & Withbroe, G. L. 1972, ApJ, 176, 511
Myint-U, T., & Debnath, L. 2009, Linear partial differential equations for scientists and engineers (Boston: Birkhäuser)
Neukirch, T. 2015, INTRODUCTION to the THEORY of MHD EQUILIBRIA (CreateSpace Independent Publishing Platform)
Neukirch, T., & Rastätter, L. 1999, A&A, 348, 1000
Neukirch, T., & Wiegelmann, T. 2019, Sol. Phys., 294, 171
Obridko, V. N., & Solov'ev, A. A. 2011, Astronomy Reports, 55, 1144
Parker, E. N. 1968, ApJ, 154, 57
—. 1979, Cosmical magnetic fields. Their origin and their activity
Pelouze, G., Auchère, F., Bocchialini, K., et al. 2021, arXiv e-prints, arXiv:2110.09975
Petrie, G. J. D., Gontikakis, C., Dara, H. C., Tsinganos, K., & Aschwanden, M. J. 2003, A&A, 409, 1065
Petrie, G. J. D., Vlahakis, N., & Tsinganos, K. 2002, A&A, 382, 1081
Piantschitsch, I., & Terradas, J. 2021, A&A, 651, A67
Piantschitsch, I., Terradas, J., & Temmer, M. 2020, A&A, 641, A21
Piantschitsch, I., Vršnak, B., Hanslmeier, A., et al. 2018a, ApJ, 857, 130
—. 2018b, ApJ, 860, 24
Pizzo, V. J. 1986, ApJ, 302, 785
Priest, E., & Forbes, T. 2007, Magnetic Reconnection
Priest, E. R. 1982, Solar magneto-hydrodynamics
Rosner, R., Tucker, W. H., & Vaiana, G. S. 1978, ApJ, 220, 643
Sakurai, T. 1982, Sol. Phys., 76, 301
Schmidt, H. U. 1964, On the Observable Effects of Magnetic Energy Storage and Release Connected With Solar Flares, Vol. 50, 107
Sewell, G. 2018, Solving Partial Differential Equation Applications with PDE2D (Newark, NJ: John Wiley & Sons)
Tsinganos, K. 2010, Memorie della Societa Astronomica Italiana Supplementi, 15, 102
Tsinganos, K., Trussoni, E., & Sauty, C. 1992, in NATO Advanced Study Institute (ASI) Series C, Vol. 373, The Sun: A Laboratory for Astrophysics, ed. J. T. Schmelz & J. C. Brown, 349
Tsinganos, K. C. 1981, ApJ, 245, 764
—. 1982, ApJ, 252, 775
Viall, N. M., & Klimchuk, J. A. 2011, ApJ, 738, 24
—. 2012, ApJ, 753, 35
—. 2016, ApJ, 828, 76
—. 2017, ApJ, 842, 108
Warren, H. P., Winebarger, A. R., & Brooks, D. H. 2012, ApJ, 759, 141
Warren, H. P., Reep, J. W., Crump, N. A., et al. 2020, ApJ, 896, 51
Webb, G. M., Brio, M., & Zank, G. P. 1994, Journal of Plasma Physics, 52, 141
—. 2001, Journal of Plasma Physics, 65, 255
Wiegelmann, T., & Solanki, S. K. 2004, SolPhys, 225, 227